Testing of the Chamber for Light Ion Detection

Laboratory of Cyclotron and Fast Neutron Generators

Martin Ansorge

Proposal ID

460

Final report regarding the proposal „Testing of the Chamber for Light Ion Detection“

M. Ansorge, J. Novák, M. Majerle, Nuclear Physics Institute of the CAS, Rez, Czech Republic

Motivated by gas production in construction materials of future fusion-related facilities as well by the basic research of nuclear reactions new detection system is under development at NPI of the CAS in recent years. The chamber is equipped with dE-E Si-detector telescopes for distinguishing between charged particle types. The CAEN V1730 digitizer is used for data acquisition. In figure 1 the vacuum chamber is shown during the preparations on the on-beam tests of electronics.

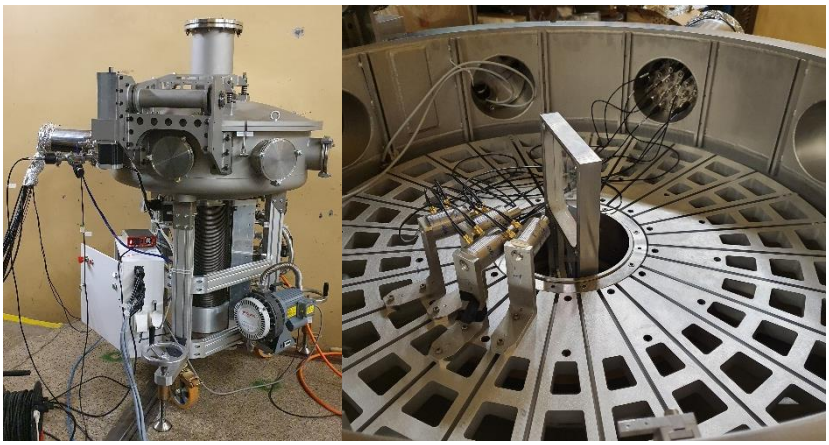

Figure 1 shows the typical experimental setup during the on-beam tests. Telescopes with Si-detectors are placed around the central sample-holder.

Days-lasting measurements with several irradiations of PE, C, Al samples were successfully performed, and the acquisition chain was finalized. The signal-noise ratio of detectors was suppressed by additional electro-magnetic shielding of preamplifiers. The detection system exhibited a good ability to measure the energy distribution of charged particles and the reasonable separation of particle types was achieved, see figure 2. It was shown that the time resolution of detected events is sufficient for usage the ToF technique and ToF method was successfully implemented.

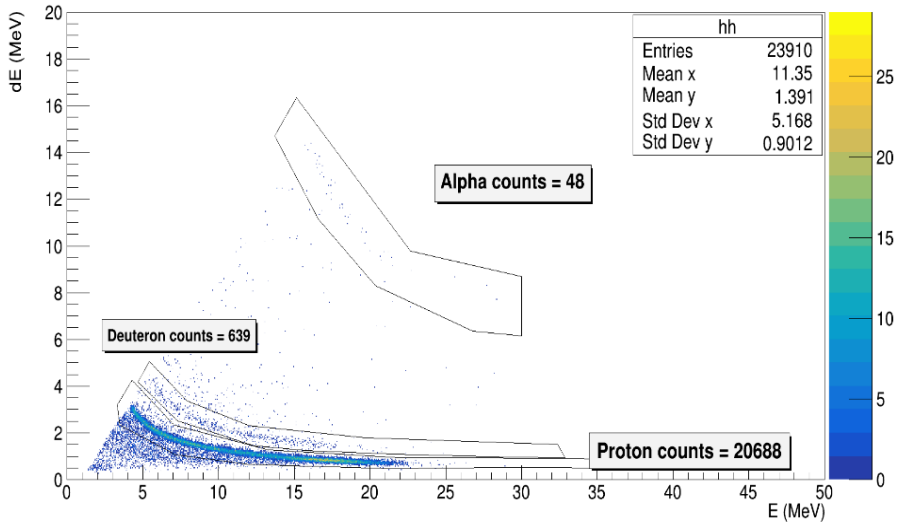

Figure 2 shows the dE-E plot of detected charged-particle-events from the six hours long irradiation of the PE target foil (thickness of 180 um, diam 3 cm) which was mounted into the central position of the vacuum chamber.

Many challenges are still ahead of us but the measurements that have been made provided us with very useful data which are used as feedback for detection electronics enhancements as well as for the development of a comprehensive software framework for data analysis in measurements of double-differential cross-sections for reactions (n, cp) induced by fast neutrons.

Identification of microscopic uranium particles using fission tracks in solid detectors

Neutron Physics Laboratory - Nuclear analytical methods with neutrons

Jan Lorincik

Proposal ID

332

Report regarding proposal " **Identification of microscopic uranium particles using fission tracks in solid detectors"**

J. Lorinčík, K. Sihelská, K. Řezanková, F. Sus, Vl. Strunga, J. Kučera

The goals of this project were (A) the study of the number of fission tracks as a function of enrichment and size of U-particles, (B) the optimization of the fission track (FT) procedure for higher reproducibility, robustness, and accuracy.

A quantitative relation between the U-particle enrichment, size, and the number of FTs was used in the following form *[1]*: $N_T = N_{235} \cdot \sigma_f \cdot \varepsilon \cdot t \cdot \phi_{therm}$ … (1) , where N_T denotes the number of fission tracks; N_{235}, the number of ^{235}U atoms in a particle; σ_f, the fission cross section for ^{235}U [586 b]; ε, the registration efficiency (0,4); t, the irradiation time [120 s]; Φ_{therm}, the flux of thermal neutrons [3,2 x 10^{13} $cm^{-2}s^{-1}$]. Then, N_{235} can be obtained from $N_{235} = 3 \cdot (\rho_{U3O8} \cdot V_P)/M_{U3O8} \cdot N_A \cdot A_{235}/100$ … (2), where ρ_{U3O8} is U_3O_8 particle density [8,3 g/cm^3], V_P volume of the particle [cm^3], M_{U3O8} the molar mass of U_3O_8 [842,1 g/mol], N_A the Avogadro's constant, A_{235} the enrichment [%]. Constant 3 in eq. (2) corresponds to the number of U atoms in U_3O_8 molecule. Since SEM images can provide only areas of 2D projections (characterized by equivalent circle diameter – d_{ECD}) of 3D shapes of particles, the geometry models, e.g. sphere, cylinder, cube must be used for *Vp* estimation.

For experimental work, standard reference materials of U_3O_8 were used: CRM 129-A (NU), CRM 010 (1% ^{235}U enriched), CRM 030-A (3% ^{235}U enriched). Then FT sample assemblies (see more detail in reports of project CANAM:ID241) were prepared and irradiated in the reactor LVR-15 with irradiation parameters specified above. After etching of the Lexan detectors, optical images were made (see Fig. 1 a-c) and the FTs manually counted. The comparison of theoretical estimates and experimental data (lines vs. data points) is in Fig. 1 d.

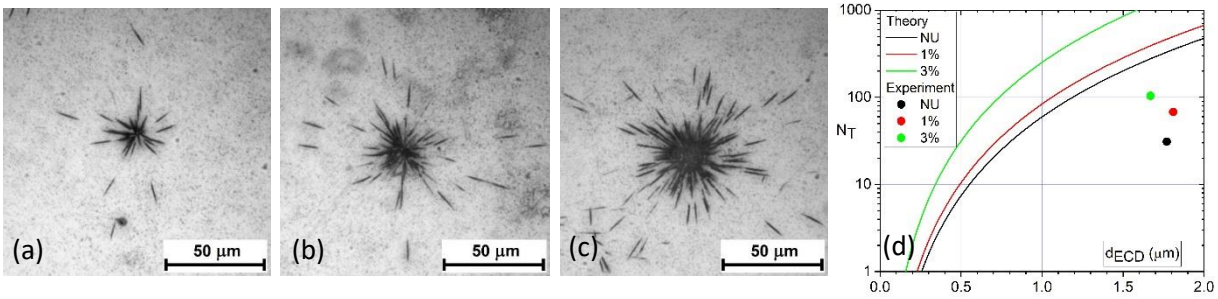

Figure 1.Optical images of FTs corresponding to U_3O_8 particles of NU (a),1 %U (b),and 3%U (c) [2]. Number of registered FTs in the images (a)-(c) for NU, 1%U, 3%U is 31, 68, 104, resp. (d) Comparison of experimental values (circle symbols) and theoretical estimates (full lines) based on equations (1) and (2) for spherical geometry model ($V_P = \pi/6 \cdot d_{ECD}^3$).

In parallel to the above study, large effort has been spent on improvement of the FT procedure. This goal has been achieved by (i) reconfiguration of the fiducial marks for better particle position precision, (ii) addition of sticky collodion for better particle adhesion, (iii) redesigning of the FT sample assembly for simpler and more reliable manipulation, (iv) employing new optical microscope with motorized stage for automated creation of compound photos of large areas of the Lexan detector, and (v) implementing efficient coordinate transformation algorithm for transfer of particle coordinates between instruments.

In summary, the dependence of the number of FTs on the particle enrichment and size has been investigated both theoretically and experimentally. There is a discrepancy between the theoretically predicted numbers of FTs and the counts of FTs obtained from the experiment. A combined effect of overestimated values of neutron fluences, material density, and FT registration efficiency could have been responsible for that. More experiments are needed to support that explanation and to provide more accurate data for theoretical predictions.

The main outcome of this project is substantial improvement of the FT procedure, which achieved the readiness level that allowed for the proficiency testing for nuclear safeguards.

[1] O. Stetzer, et al, . Nucl. Instr. Meth. Phys. Res. A525 (2004), pp. 582-592.
[2] S. Konegger-Kappel, et al https://www.iaea.org/sites/default/files/19/07/cn-267-book-of-abstracts.pdf, CN267-226, pp.228.

Characterization of Residual Stresses Distribution in Laser Cladded H13 tool steel

Neutron Physics Laboratory - Neutron diffraction

Karel Trojan

Proposal ID

461

Report regarding proposal "Characterization of Residual Stresses Distribution in Laser Cladded H13 Tool Steel"

K. Trojan [1,a], D. Canelo-Yubero[2], J. Čapek [1], N. Ganev [1]

[1] Department of Solid State Engineering, Faculty of Nuclear Sciences and Physical Engineering, CTU in Prague, Trojanova 13, 120 00 Prague 2, Czech Republic
[2] Department of Neutron Physics, Nuclear Physics Institute, ASCR, v.v.i., 25068 Řež, Czech Republic
[a] karel.trojan@fjfi.cvut.cz

Laser cladding was carried using a IPG 3kW Yt:YAG fibre laser and powder of the AISI H13 tool steel. Five-layer sample was formed from six and seven overlapping beads on the substrate made from AISI H11 tool steel. The state of residual stress and the dependence of the FWHM parameter were described using neutron diffraction in the middle of the sample in the plane perpendicular to cladding.

It was found from the measured residual stresses in three different sample orientations (see Fig. 1) that the greatest gradient of residual stresses (RS) is in the direction normal to the surface (N – normal direction). According to the literature study [1, 2], the maximum residual stresses are located 4 mm below the surface and compressive stresses prevail in the T direction. The substrate, on the other hand, exhibits tensile residual stresses. According to our results in the clad itself in the T direction, tensile RS predominate, on the contrary, in the substrate compressive RS with one maximum of tensile RS approximately 3 mm below the surface of the substrate were determined.

Laser deposition of the H13 tool steel showed a great application potential. The obtained results will help to understand the development of residual stresses within the thickness of the newly formed material. This knowledge can be used to design a procedure for laser beam deposition of larger volumes.

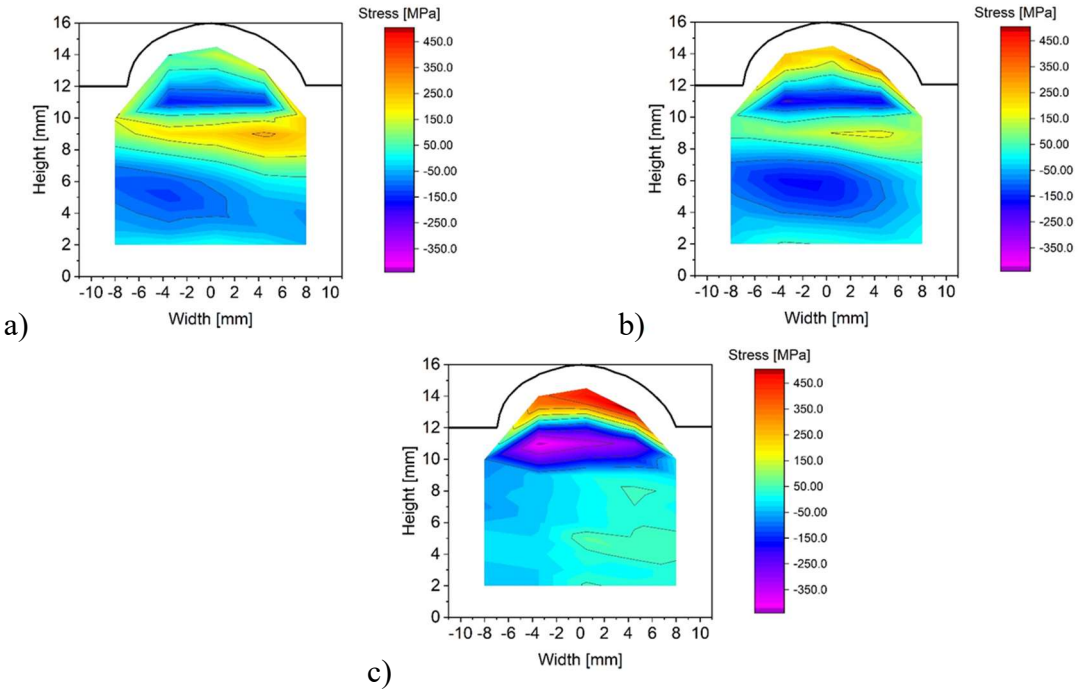

Fig. 1: Map of bulk residual stresses in the cross section of the clad in a) L, b) T and c) N direction.

Reference

[1] Cottam, R., Wang, J., & Luzin, V. (2014). Characterization of microstructure and residual stress in a 3D H13 tool steel component produced by additive manufacturing. Journal of Materials Research, 29(17), 1978-1986. doi:10.1557/jmr.2014.190

[2] Bailey, N., Katinas, C., & Shin, Y. (2017). Laser direct deposition of AISI H13 tool steel powder with numerical modeling of solid phase transformation, hardness, and residual stresses. Journal of Materials Processing Technology, 247, 223-233.

Advanced organic-inorganic nanostructures

Laboratory of Tandetron

Vladimir Cech

Proposal ID

466

Report on the project "Advanced organic-inorganic nanostructures"

V. Cech, Inst. Mater. Chem., Brno Univ. Technol., Brno, Czech Republic
A. Romanenko, A. Mackova, Nucl. Physics Inst., Rez, Czech Republic

The main task of the proposed experiment was to provide an elemental analysis of polymer-like hydrogenated amorphous carbon-silicon (a-CSi:H) films using RBS and ERDA. The polymer-like a-CSi:H films were deposited from the tetravinylsilane (TVS) precursor by continuous wave (low-pressure plasma-enhanced chemical vapor deposition, LP PECVD) at an extremely low RF power of 0.2 W. These films were found to be unstable under ambient conditions and subject to post-deposition oxidation. The polymer-like film must therefore be overcoated with a 6-8 nm thick barrier layer to protect it and prevent degradation. A compact a-CSi:H film with a density of 2.0 g/cm^3 was successfully used as a barrier (XPS depth profiling), which was deposited from the TVS/Ar mixture by pulsed plasma at 25 W. To optimize the elemental analysis and increase the sensitivity to light elements, the films were deposited only on glassy carbon as a substrate. Further ERDA measurements showed a problem with the sputtering of polymer-like film and therefore it was necessary to optimize the ERDA charge per measurement. The areas affected by irradiation are visible to the eye as the charge was gradually reduced by 7.4, 3.7, 1.48, and 0.74 μC per measurement, see Fig. 1.

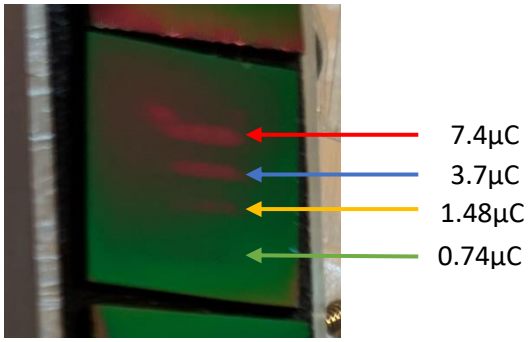

Fig. 1. Photo of the polymer-like film after testing in (a) ERDA geometry and (b) RBS measurements.

Although the ERDA charge was only 0.37 μC per measurement and 20 consecutive measurements were made at one location (the angle of incidence was 75°), the film on the surface is subject to changes during irradiation. It was found that both the thickness and the hydrogen concentration are reduced. Using an RBS charge of 0.74 μC per measurement (the angle of incidence was 7°), 10 measurements in a row were performed at one location. The final ERDA and RBS spectra corresponding to a charge of 0.74 μC can be seen in Fig. 2. The composition of the film (atomic [mass] concentration) is as follows: Si 7[28.2]%, C 37[63.8]%, H 56[8]%. The film thickness of 6200×10^{15} at/cm^2 corresponds to a thickness of 591 nm (measured by spectrometric ellipsometry) when a density of 1.2 g/cm^3 is used (GISA program).

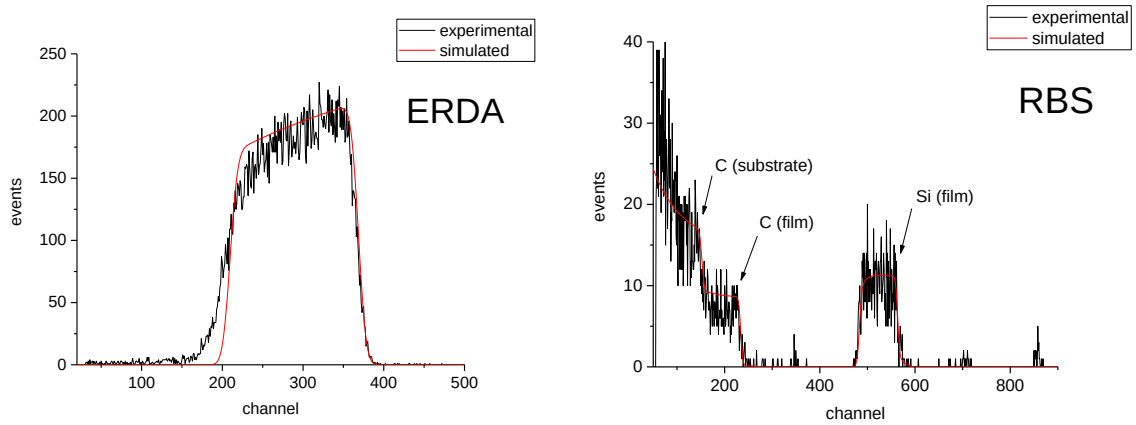

Fig. 2. ERDA and RBS spectra of polymer-like film corresponding to a charge of 0.74 μC.

Careful analysis of polymer-like a-CSi:H films is important for the further construction of layered nanostructures combining the polymer-like and oxygen bound a-CSiO:H films.

Effects of radiation-induced damage on light ions diffusion in ISOL-related targets

Laboratory of Tandetron

Antonino Cannavó

Proposal ID

530

Report regarding proposal "Effects of radiation-induced damage on light ions diffusion in ISOL-related targets"

Antonino Cannavó, Vladimír Havránek and Jiří Vacík

Methods

In the experiment, molybdenum foils with a thickness of 50 μm were implanted at room temperature with $^6Li^+$ ions with energy 390 keV with a fluence of about 10^{16} cm^{-2}. The implantation was carried out at the Helmholtz-Zentrum Dresden-Rossendorf (HZDR) at the 3 MV Tandem accelerator. The $^6Li^+$ ion beam current density was about 10-25 nA/cm^2 corresponding to the thermal power density between 4 to 12 mW/cm^2. After implantation of $^6Li^+$ (in HZDR Dresden), a part of the Mo(^{6}Li) samples was irradiated by 12 MeV $^{12}C^{4+}$ ions with a fluence of 10^{14} cm^{-2} at the 3 MV Tandetron accelerator in the NPI Řež. The aim was to generate radiation defects in the Mo(^{6}Li) foils, which should lead (due to radiation-induced diffusion) to redistribution of the ^{6}Li dopants. However, because of the possible heating effect, caused by the $^{12}C^{4+}$ ion bombardment, it was necessary to prevent the sample temperature from rising, which would otherwise also induce unwanted Li diffusion. Therefore, the Mo(^{6}Li) foils were irradiated only with a low current of about 10 nA/cm^2, so the temperature on the sample (measured in situ by a K-type thermocouple, did not exceed 40 °C throughout the monitoring period.

Results

The ^{6}Li depth profiles in the Mo(^{6}Li) foils before (Pristine) and after $^{12}C^{4+}$ irradiation (Irradiated) were measured by the NDP method at the research reactor LVR-15 in Řež (operated by the Research Center Řež). When determining the residual energies of α-particles and tritons for thermal neutron-induced reaction, the depth position of their parent atoms (^{6}Li) in the Mo(^{6}Li) foils can be evaluated. For this purpose, the MC LIBOR code was developed, using the SRIM database, which allows reconstruction of the ^{6}Li depth profiles in solids.

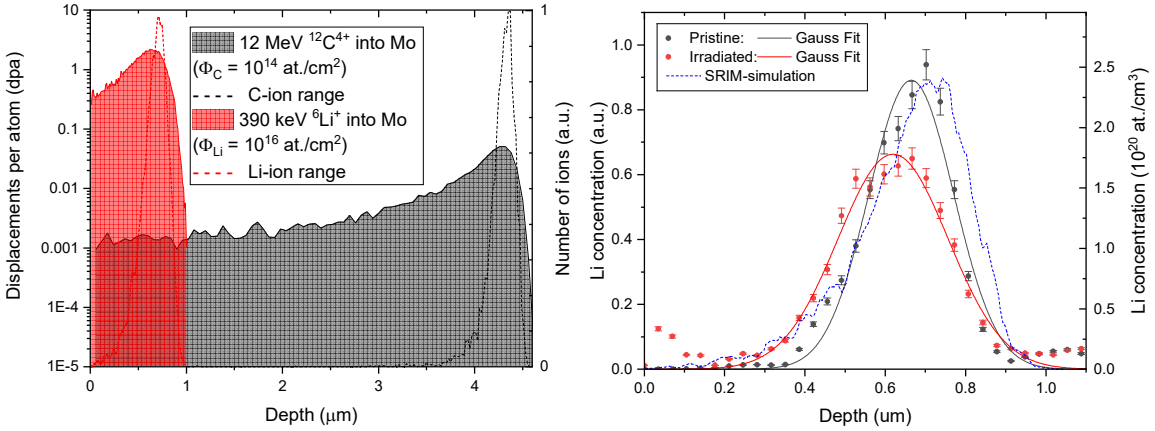

Figure 1: Left: SRIM simulations of ions range (dashed lines) and damage in dpa units (area under curves) for 390 keV $^6Li^+$ and 12 MeV $^{12}C^{4+}$ ions, in red and black colors, respectively. Right: SRIM simulation and Li-depth profiles for Pristine and Irradiated samples with the corresponding Gaussian fits.

Irradiation conditions in both 390 keV $^6Li^+$ ion implantation and 12 MeV $^{12}C^{4+}$ ion irradiation were first inspected by the SRIM code. Fig. 1 (left) shows the result of the SRIM simulation. The simulation shows that the range of $^6Li^+$ ions (660 nm) in Mo is significantly smaller than that of $^{12}C^{4+}$ ions (4280 nm), and that the radiation damage (expressed as the equivalent displacement dose, D), caused by the carbon ion bombardment, is approximately the same ($\sim 1.5 \times 10^{-3}$ dpa) throughout the entire passage of the $^6Li^+$ ions in Mo. On the other hand, the destructive effect of Li ions is concentrated on the narrow subsurface region of the Mo foil, and for a thickness T as less as 660 nm, the D is greater (~2.16 dpa) than for $^{12}C^{4+}$ ions. The deconvolution of the NDP spectra into Li-depth profiles is shown in Fig. 1 (right). The FWHM parameter, characterizing the Gaussian-like depth profile distributions, increased from the original value of 249 nm (for Pristine) to 320 nm (for Irradiated), which demonstrates the RID effect after bombardment (12 MeV $^{12}C^{+4}$, $\Phi_C = 10^{14}$ cm^{-2}). In addition, the centroid of the Gaussian curves has shifted from 665 nm to 619 nm.

Characterization of lithium mobility in glass-ceramic LICGC solid electrolyte

Neutron Physics Laboratory - Nuclear analytical methods with neutrons

Antonino Cannavó

Proposal ID

531

Report on the experiment:

Characterization of lithium mobility in glass-ceramic LICGC solid electrolyte

Antonino Cannavó, Ivo Tomandl, Giovanni Ceccio, Jiří Vacík.

The NDP method proved to be a unique tool for the study of lithium transportation (migration and diffusion) in the Solid Electrolyte (SE). The experiment has pointed out the formation of a lithium depleted region in the interface between the LICGC SE and Au/Cu current collector. In particular, it was observed how the phenomenon occurs in relation to the applied voltage and time.

The formation of the Li -depleted region at the SE/Cu interface results in a variation of the NDP spectra in the channel range between 850 and 1000. This region of the spectrum corresponds to the most energetic tritons, generated close by the sample surface: Fig. 1a shows that the longer the applied voltage the smaller the area subtended by the spectrum, clearly pointing at the depletion of lithium atoms.

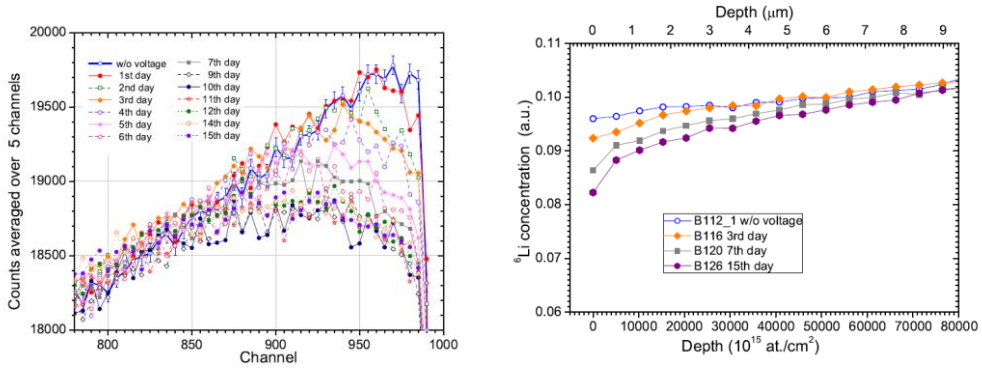

Fig.1: a) detail of the NDP spectra in the channel range between 800 and 1000; all the spectra are normalized to the same neutron fluence. b) corresponding Li-depth profile evaluated by LIBOR simulation code.

Data analysis was performed by using the LIBOR simulation code [1]. Fig. 1b shows that a consistent trend is being observed in the Li-depth profile estimated in the selected area as well.

The collected data have been used in the preparation of a paper, that now is under consideration for publication in an impacted journal.

This is the first experiment to describe the actual distribution of Li atoms in the process of forming the space charge layer. Further steps to better understand the mechanism of lithium migration and diffusion in LICGC will involve new voltage cycling strategies (negative biasing), as well as, the combination of NDP data with complementary methodologies, e.g. Rutherford Backscattering Spectroscopy or gamma-rays Spectroscopy, for a comprehensive understanding of the Li-depleted region formation at the SE interface.

References

[1] Hnatowicz, V., J. Vacik, and D. Fink. "Deconvolution of charged particle spectra from neutron depth profiling using Simplex method." Review of Scientific Instruments 81.7 (2010): 073906.

Neutron depth profiling and PIXE/PIGE comparative study on Li distribution in mixed cathodes of oxid

Neutron Physics Laboratory - Nuclear analytical methods with neutrons

Stefan Seidlmayer

Proposal ID

532

Report regarding proposal “Neutron depth profiling and PIXE/PIGE comparative study on Li distribution in mixed cathodes of oxide (LLZO-LCO) based all-solid-state batteries”

Stefan Seidlmayer, Thien-An Pham, Ivana Pivarnikova, Lukas Grossmann, MLZ (Heinz Maier-Leibnitz Zentrum, Technical University Munich, Germany)
Martin Finsterbusch, Forschungszentrum Jülich GmbH, Institut für Energie- und Klimaforschung (IEK), Jülich, Germany
Antonino Cannavo, Giovannia Ceccio, Jiri Vacik, Nucl. Physics Inst. CAS, Rez, Czech Republic

Here we investigated samples of all-solid state battery cells brought to different states of charge and a reference sample being a pure LLZO pellet of solid electrolyte material. The conducted measurements used the NDP spectrometer in the Center of Accelerators and Nuclear Analytical Methods (CANAM) infrastructure of the Nuclear Physics Institute (NPI) CAS in Rez, Czech Republic. Due to the Covid-19 pandemic, NPI instrument responsible scientists carried out the experiments remotely. The measurements used two setups: the A-Line with an inserted 2.8 µm Macrofol filter and B-Line without any filter. Calibration to energy and Li-concentration was performed with a ^{6}LiF standard (see fig. 1) measured in both Line setups. Data analysis for the complex full cell samples is ongoing. The expected nuclear reaction of interest for the lithium depth profiles is ^{6}Li(n, ^{3}H)^{4}He, which generates two particles of interest, namely Triton ($^{3}H^{+}$) and alpha ($^{4}He^{2+}$) particles with different recoil energies of 2727 keV (^{3}H) and 2055 keV (^{4}He), respectively. The lithium depth profiles are calculated with the N4DP software package [1, 2], which applies the stopping power of the atomic composition of the sample simulated by the SRIM software [3] on the energy calibrated data set. The evaluation assumes a constant average density across the layers of interest. The abundance of ^{6}Li was set to the natural value of 7.59% according to IUPAC [4]. Figure 2 shows the obtained Li depth-profiles obtained by using the N4DP software package implementing SRIM-data for the data treatment. For B-Line, the data treatment assumed an 80 nm thick Si dead layer of the detector and for A-Line an additional 2.8 µm thick Macrofol passive layer. Finally, we applied a sample specific calculation for the active layer SRIM-profile. For sample #5, a pellet of pure LLZO material we assumed a homogenous average composition $Li_{6.6}Al_{0.15}La_3Zr_{1.58}Hf_{0.02}Ta_{0.4}O_{12}$ with an average density of 4.924 g/cm^3. Preliminary inspection of the data suggests a very homogenous Li distribution. The accessible depth of the LLZO pellet is approximately 20 µm. Interestingly, there is an unexpected surface peak in both signals, i.e. Triton and Alpha particles, indicating a possible Li-gradient up to a depth of 300 – 400 nm, which could point towards a concentration gradient in the LLZO-particles, decreasing from shell to core.

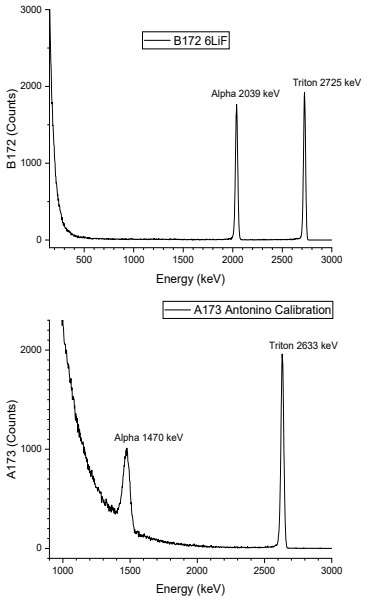

Fig. 2: NDP spectra of the ^{6}LiF standard measured on the A- and B-Lines.

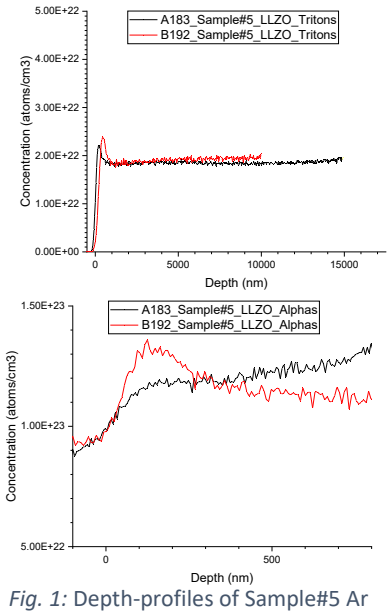

Fig. 1: Depth-profiles of Sample#5 Ar annealed LLZO-Pellet. Top: Triton particles; Bottom: Alpha particles;

References

1. Werner, L., Trunk, M., Gernhäuser, R., Gilles, R., Märkisch, B. and Révay, Z., 2018, Nuclear Instruments and Methods in Physics Research Section A: Accelerators, Spectrometers, Detectors and Associated Equipment, 911, 30-36.
2. Trunk, M., Wetjen, M., Werner, L., Gernhäuser, R., Märkisch, B., Révay, Z., Gasteiger, H. A. and Gilles, R., 2018, Materials Characterization, 146, 127-134.
3. Ziegler, J. F., Ziegler, M. D. and Biersack, J. P., 2010, Nuclear Instruments & Methods in Physics Research Section B-Beam Interactions with Materials and Atoms, 268(11-12), 1818-1823.
4. Meija, J., Coplen, T. B., Berglund, M., Brand, W. A., Bièvre, P. D., Gröning, M., Holden, N. E., Irrgeher, J., Loss, R. D., Walczyk, T. and Prohaska, T., 2016, Pure and Applied Chemistry, 88(3), 293-306.

Investigate the structures of Na-ion cathode materials

Neutron Physics Laboratory - Neutron diffraction

Neelima Paul

Proposal ID

534

Research question: In our work, we want to elucidate the influence of the charge ordering in the transition metal slab on the sodium/vacancy ordering within the sodium slab of the material. We have synthesised both phase-pure materials, P2-$Na_xNi_{1/3}Mn_{2/3}O_2$ and P2-$Na_{2/3}Ni_{1/4}Mn_{3/4}O_2$, and used electrochemical methods as well as X-ray diffraction to investigate sodium/vacancy orderings in these materials. Both materials exhibit sodium/vacancy orderings at the reported compositions. To characterise the ordering of manganese and nickel within the transition metal slab, neutron powder diffraction measurements have been performed at Meredit.

Obtained data and analysis: The obtained neutron powder diffraction patterns of the three samples measured at Meredit, $Na_{2/3}Ni_{1/3}Mn_{2/3}O_2$, $Na_{2/3}Ni_{1/4}Mn_{3/4}O_2$ and $Na_{0.59}Ni_{1/4}Mn_{3/4}O_2$, are represented in Figure 1.

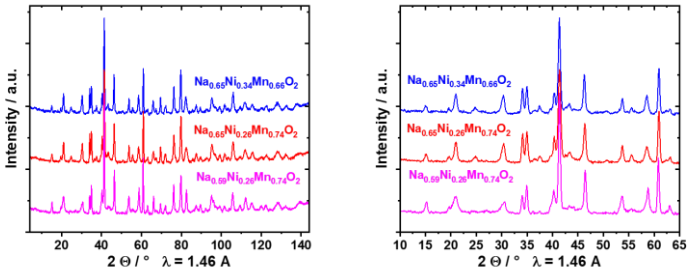

Figure 1: NPD patterns measured at Meredit. (left) complete data set, (right) zoom-in for identification of superstructure.

The diffraction patterns of all three samples exhibit additional reflections (between 18°–28° 2Θ) compared to X-ray patterns that can be indexed using the superstructure with propagation vector ***k***=(1/3 1/3 0). This superstructure is created by ordering the nickel-manganese in the honeycomb sub-lattice. The order is revealed in diffraction data thanks to the different neutron scattering lengths of Ni and Mn.
Three different stacking sequences of the identified nickel-manganese orderings are reported in literature[8,9]: (i) A-A stacking, (ii) A-B stacking or (iii) a mixture of both (stacking faults). All three options were examined, and the analysis suggests that the A-B stacking dominates.

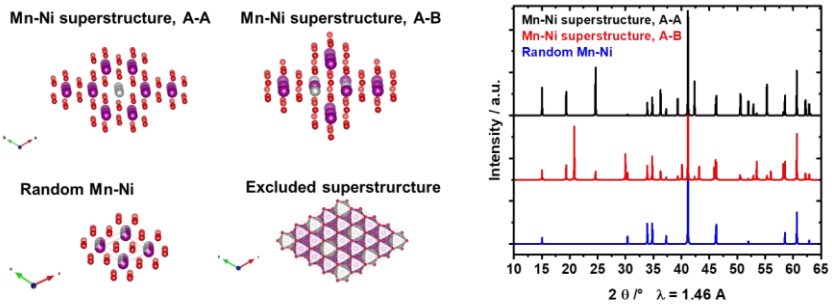

Figure 2: (left) Possible transition metal superstructures and stacking sequences. (right) Simulated NPD data using PowderCell. Refinement of the NPD data suggests that the honeycomb Mn-Ni ordering with A-B stacking sequence is dominant in all three samples.

Additional broadening of (10*l*) reflections is identified in NPD and XRD data. This anisotropic broadening most likely results from two-dimensional stacking faults within the layered structure. We are currently evaluating possible two-dimensional stacking faults and implementing these in the software Faults[10] (part of FullProf). The simultaneous analysis of NPD and XRD data with these models is ongoing.
So far, the best results are obtained by incorporating (2/3 1/3 1/2 translations, leading to a different prismatic sodium environment and different stacking of the transition metals.

Investigation of Li distribution in Si/C composite anodes from Li-ion batteries at selected SOHs

Neutron Physics Laboratory - Nuclear analytical methods with neutrons

Ivana Pivarníková

Proposal ID

536

Experimental report for the Proposal ID 536:

Investigation of Li distribution in Si/C composite anodes from Li-ion batteries at selected SOHs

Ivana Pivarníková, Neelima Paul, Ralph Gilles (Heinz Maier-Leibnitz Zentrum (MLZ), Technical University Munich, Germany)
Marius Flügel, Christin Hogrefe, Thomas Waldmann (Zentrum für Sonnenenergie- und Wasserstoff- Forschung Baden-Württemberg (ZSW), Ulm, Germany)
Jiří Vacík (Nuclear Physics Institute, Rez, Czech Republic)

Neutron depth profiling measurements of Si/Graphite (Si 3.53 wt.%, C 96.47 wt.%, 1.58 g/cm^3) electrodes extracted from Li-ion batteries were performed at the T-NDP instrument. The electrodes were at different states of health (SOH) and previously aged under various conditions in order to investigate the influence of these parameters on the lithium depth profiles. The following 4 samples were measured: B146 (fresh electrode, SOH 100%), B147 (SOH 90%, aging at 45°C, with SEI formation), B148 (SOH 76%, aging at 45°C, with SEI formation), and B149 (SOH 60%, aging at 0 °C, with induced Li plating). Additionally, 3 different reference samples were measured: B150 (^{6}LiF), which was used for energy calibration, B152 (NIST standard RR4N16, 1.094E16 atom/cm^2 of ^{10}B atoms), which was used for quantity calibration, and B151 ($LiNbO_3$, 417 nm), which was used as an additional reference for crosschecking the analysis. The nuclear reaction of interest for the neutron depth profile is ^{6}Li(n,^{4}He)^{3}H, which creates two particles of interest: triton (^{3}H) and alpha (^{4}He) with their respective recoil energies of 2727 keV (^{3}H) and 2055 keV (^{4}He). For the thin reference sample ^{6}LiF, the signal is well defined and therefore can be used for energy calibration, as we can observe on the energy spectrum in Fig. 1a. In Fig. 1b, we can observe the energy spectra of $LiNbO_3$. For the NIST standard sample, the reaction of interest is ^{10}B(n,^{4}He)^{7}Li and we can observe the energy spectra in Fig. 1c. The peak positions are shifted in comparison to the theoretical values of the reactions due to implantation of ^{10}B into the Si substrate. However, this does not affect the suitability of the sample for quantity calibration of the Li content.

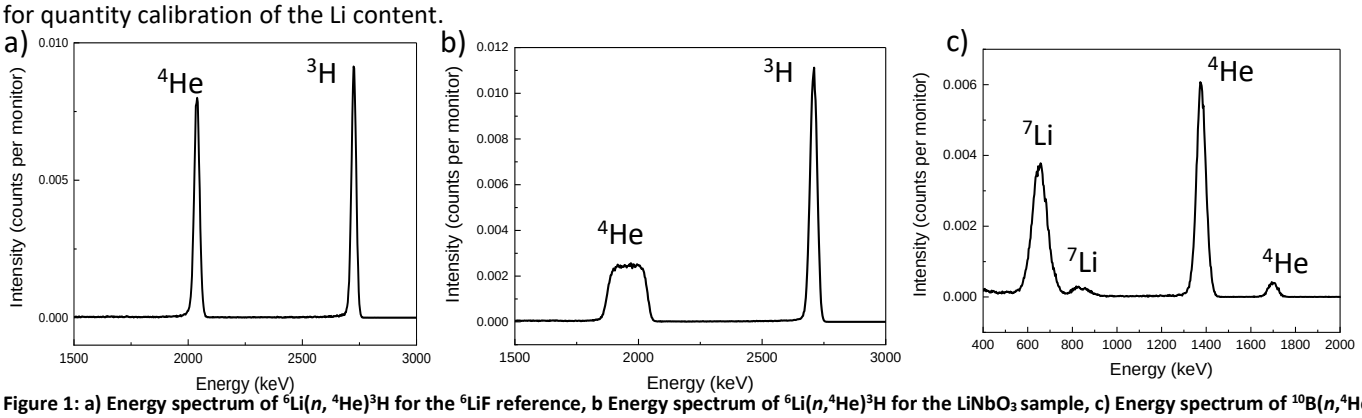

Figure 1: a) Energy spectrum of ^{6}Li(n, ^{4}He)^{3}H for the ^{6}LiF reference, b Energy spectrum of ^{6}Li(n,^{4}He)^{3}H for the $LiNbO_3$ sample, c) Energy spectrum of ^{10}B(n,^{4}He)^{7}Li for the NIST boron standard.

The depth profile analysis is done by N4DP software [1], which uses the energy loss of ions in matter calculated by the SRIM software [2] on the energy-calibrated data. A constant average density across the various layers is assumed for each sample. A natural isotopic abundance of 7.59% for ^{6}Li is assumed to calculate the total lithium concentration [3]. We can observe the energy spectra of our 4 measured samples in Fig. 2a. There is a clear overlap of alpha and triton signal, because of the higher thickness of electrodes (≈80 µm). Therefore, the available depth for our measurements is limited to approximately 16 µm (corresponding to a triton spectrum between 2075 and 2055 keV), as seen in Figure 2b, which also shows the final depth profiles of the Li distribution in the electrodes. We can observe increasing Li concentration with a decreasing SOH of the electrodes. Moreover, the highest peak (B149) corresponds to the electrode with charging conditions inducing Li-plating on the electrode surface, as was expected. As planned, these results were compared with the results from GD-OES (glow discharge optical emission spectroscopy) depth profiling method. It turns out that the Li depth profiles from both methods are in good agreement. The publication of these results is currently in preparation.

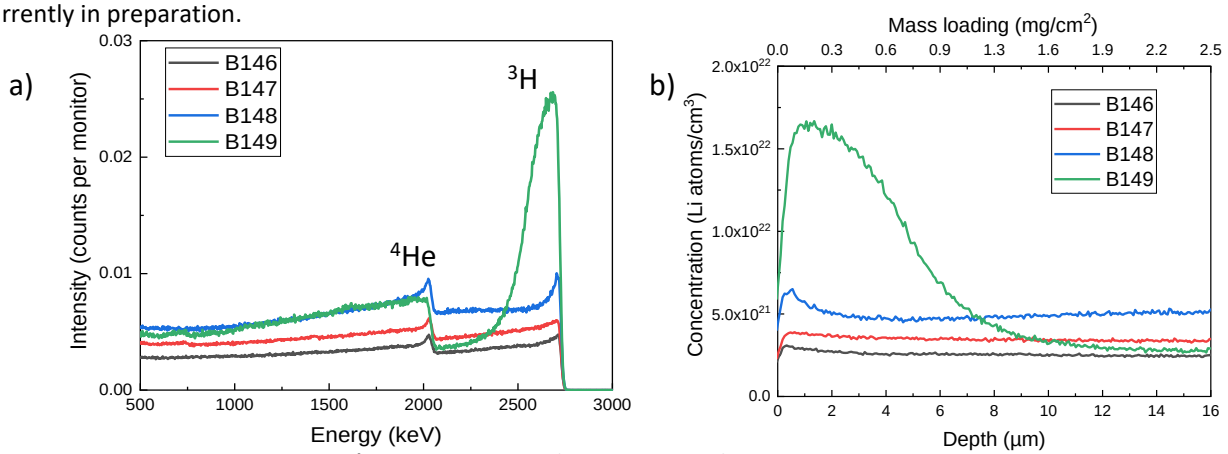

Figure 2: Results for four different types of Si/Graphite electrodes: a) Energy spectra, b) Lithium concentration profiles as a function of electrode depth.

[1] Trunk, M., Wetjen, M., Werner, L., Gernhäuser, R., Märkisch, B., Révay, Z., Gasteiger, H. A. and Gilles, R., 2018, Materials Characterization, 146, 127-134.
[2] Ziegler, J. F., Ziegler, M. D. and Biersack, J. P., 2010, Nuclear Instruments & Methods in Physics Research Section B-Beam Interactions with Materials and Atoms, 268(11-12), 1818-1823
[3] Meija, J., Coplen, T. B., Berglund, M., Brand, W. A., Bièvre, P. D., Gröning, M., Holden, N. E., Irrgeher, J., Loss, R. D., Walczyk, T. and Prohaska, T., 2016, Pure and Applied Chemistry, 88(3), 293-306.

Unveiling the Lithium Depth Profile Upon Lithiation of Silicon-Based Anodes

Neutron Physics Laboratory - Nuclear analytical methods with neutrons

Lukas Grossmann

Proposal ID

538

Report regarding proposal ID 538: “Unveiling the Lithium Depth Profile Upon Lithiation of Silicon-Based Anodes”

Lukas Grossmann, Thien-An Pham, Stefan Seidlmayer, Phillip Rapp, and Ralph Gilles, Technical University of Munich (TUM), Germany
Antonino Cannavo, Giovanni Ceccio, and Jiri Vacik, Nuclear Physics Institute in Rez, Czech Republic

The usage of silicon as anode material in Lithium Ion Batteries (LIB) would lead to higher capacities as compared to common graphite anodes. However, the high volume increase of Si during lithiation leads to a low cycling stability.[1] One strategy to overcome this problem is the partial lithiation to ~30%, which results in a significant gain in cycling stability while maintaining a high capacity.[2] Homogeneous lithiation across the electrode is believed to be beneficial for the cycling stability since the stress caused by the increase in volume is evenly distributed.

We use thermal Neutron Depth Profiling (NDP) on extracted anodes to investigate the Li depth distribution after their formation and lithiation. The NDP method utilizes an intense 6Li(n, α)t reaction with a high cross section of 940 barns to measure the Li concentration vs. depth. Thereby, we use an electrode coating chemistry based on 70 wt.% of micrometer-sized Si particles. Additionally, we study the formation with and without $LiNO_3$ as electrolyte additive as it can significantly increase the cycling stability of these anodes.[3] Electrodes (Si-rich coating on Cu-collector) were packed in pouch bags with 7.6 µm thick Kapton windows to prevent contact with air and to filter out $^4He^{2+}$-particles during NDP, resulting in pure $^3H^+$-spectra. The samples were remeasured without the pouch bag after a short (few minutes) exposure to air to attain also the $^4He^{2+}$-signal.

The experiments were carried out using the NDP spectrometer in the Center of Accelerators and Nuclear Analytical Methods (CANAM) infrastructure of the Nuclear Physics Institute (NPI) in Rez, Czech Republic. The experiments had to be performed remotely due to the Covid-19 pandemic and were operated by the instrument responsible scientists.

Fig. 1 summarizes the preliminary results. The Li depth profiles are calculated based on the stopping power of the atomic composition of the electrode coating using the SRIM software.[4] In the evaluation, a constant (experimentally determined) density across the coating was assumed. The abundance of ^6Li was set to be 7.56% according to IUPAC.[5] All depth profiles measured with the Kapton filter show a homogeneous Li concentration (Fig. 1a). The low Li concentration from the pristine sample (i.e. with no electrochemical treatment) originates from the LiPAA binder used in the electrode coating. After formation, the Li concentration becomes five times higher resulting from Li irreversibly bound in the solid-electrolyte interface (SEI), which formed during the formation of the cell. With increasing lithiation state the Li concentration consistently increases. The drop in Li concentration at greater depths indicates the end of the coating. The inflection points are assumed to be the interface between the Li-containing Si-rich coating and the Cu collector. The coating was prepared homogeneously with a thickness of ~25 µm. However, the lithiation process caused a significant swelling of the coating layer, as evident from the broadening of the NDP depth profiles (see red lines and arrows in Fig. 1a). After unpacking and measuring the electrodes without the filter, the depth profiles slightly changed (Fig. 1b). It should be noted, that these profiles only make sense until the onset of the $^4He^{2+}$-signal between 30 and 40 µm. Interestingly, a dominant surface peak occurs which is an effect that has to be further evaluated. However, it indicates an enrichment of Li on the electrode surface. Furthermore, the surface peak is followed by a lowered Li concentration up to around 10 µm. Our first interpretation is that this dip is due to oxidation of the lithiated silicon. Fig. 1c compares the depth profiles of the electrodes after formation, whereby in one of the samples $LiNO_3$ was dissolved in the electrolyte as an additive. The depth profiles show a higher Li concentration in the SEI of the sample where the formation was conducted with the additive. Moreover, the intensity of the surface peaks differs. Appropriate complementary techniques as well as electrochemical measurements will be necessary to further interpret these results.

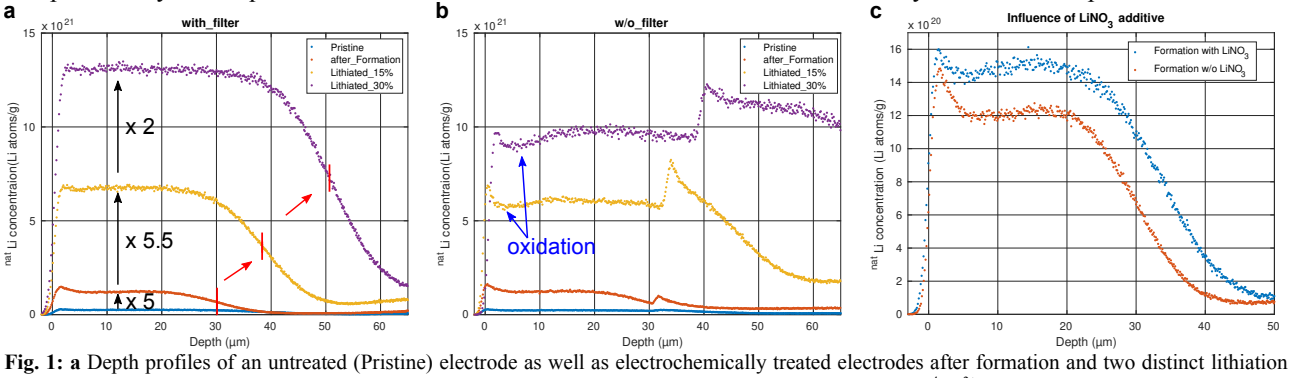

Fig. 1: a Depth profiles of an untreated (Pristine) electrode as well as electrochemically treated electrodes after formation and two distinct lithiation steps. These samples were measured through a 7.6 µm thick Kapton foil which acted as a stop-filter for the $^4He^{2+}$-particles and additionally prevented air contact of the sample prior to measurement. The swelling of the electrodes is indicated by the red lines and arrows. **b** Same samples as in a, but this time without a filter and a short air contact of the electrodes for a few minutes. The dips in the profiles ranging from appr. 2 to 10 µm as indicated by the blue arrows are interpreted as oxidation effects. **c** Comparison of two electrodes after the electrochemical formation step, once with $LiNO_3$-additive dissolved in the electrolyte and once without. These measurements were performed with a Kapton foil filter.

References

[1] Gonzalez, Joseph, et al. Journal of Power Sources 269 (2014): 334-343.
[2] Jantke, Dominik, et al. Journal of The Electrochemical Society 166.16 (2019): A3881.
[3] Haufe, Stefan, Rebecca Bernhard, and Jürgen Pfeiffer. Journal of The Electrochemical Society 168.8 (2021): 080531.
[4] Ziegler, James F., et al. Nuclear Instruments and Methods in Physics Research Section B 268.11-12 (2010): 1818-1823.
[5] De Laeter, John R., et al. Review 2000 (IUPAC Technical Report)." Pure and applied chemistry 75.6 (2003): 683-800.

Ion beam microstructuring of polymers and carbon allotropes.

Laboratory of Tandetron

Petr Malinsky

Proposal ID

475

Report regarding proposal “Ion beam microstructuring of polymers and carbon allotropes. ”

P. Malinský, A. Macková. K. Szökölová, J. Luxa, P. Slepička, V. Švorčík, Z. Sofer

The proposal was denoted to the study of ion micro-beam irradiation of graphene oxide (GO), polymethylmethacrylate (PMMA) and polyimide (PI) foils with the aim of their reducing and change electrical properties.

Graphene and graphene-like materials have aroused significant interest for supercapacitors and ultra-sensitive gas and liquid detectors because of their remarkably high carrier mobility, extraordinary surface area, 2D structure and cost-effective easy-to-prepare nanoscale morphologies [1, 2]. The cross-linked PMMA and related compounds, Pis and cellulose derivatives have been tested as sensing polymers and non-ionic polar PIs are the most commonly used group of materials for capacitive humidity sensors [3, 4]. The GO, PI and PMMA can absorb liquids or gases that occupy the free space between the polymeric and GO molecules and change its dielectric constant [5].

In our work, the GO, PMMA and PI foils were irradiated using an optimised 5 MeV C^{3+} ion beam with micrometer-scale resolution to induce the carbonisation/deoxygenation/dehydrogenation of the selected area and to enhance the local electrical conductivity. The ion fluence of 1800, 2700 and 3600 nC/mm^2 was used, for which a significant increase of electrical conductivity in GO, PI and PMMA had been reported earlier [6,7]. The irradiated samples were subsequently analyzed by ERDA, RBS, XPS, SEM and Raman spectroscopy to characterize the elemental composition, elemental depth profiles, subsurface chemical bonds and chemical composition modification as well as the surface morphology. The electrical and the sensory properties were tested in environmental chamber with varying humidity and compared with real ceramic capacitors and BME280 combined humidity sensor.

The ion irradiation in GO leads to removal of oxygen functional species and GO reduction accompanied with carbonization of irradiated parts and creation of new carbon bonds. Molecular chain scission, bond cleavages, dehydrogenation and creation of unsaturated bonds together with significant surface destruction is observed in PMMA as a result of the ion irradiation. The ion irradiation of PI leads to the oxidation of very thin surface layer, and to deoxygenation and carbonization in the deeper substrate layers. All these compositional and structural changes in irradiated parts of GO, PMMA and PI samples result in a change of electric conductivity. So that, the irradiated and well organized parts of insulators play the role of capacitor electrodes and non-irradiated parts play the work as an embedded dielectric. These prepared structures were used as capacitors and capacitive/resistive humidity sensors.

The micro-structure with the highest measured capacitance of about 4 pF was prepared on the GO surface. Unfortunately, the capacitance of the micro-structures prepared on the GO surface is evidently influenced by non-negligible conductivity of partially reduced GO between electrodes prepared by ion beam writing. The similar micro-structures prepared on the surface of PI and PMMA exhibit lower capacitance compare to the GO based one. In comparison with GO the PI exhibits much higher radiation resistance. The GO capacity change with change of humidity in atmospheric chamber. On the other side, the polymer components don’t show capacity change with varying humidity but resistance of polymer structures decrease significantly with water vapor concentration in air. In general, we show that the carbon ion micro-lithography is a simple, rapid and green method for fabrication of analog electronic micro-device fabrication need for masks, templates or post-processing.

[1] D. Zhang, et all., Sensor Actuat B-Chem 203 (2014) 263-270.
[2] A. Lamberti, et all., Nanotechnology 28 (2017) 174002.
[3] M. Matsuguchi,et all., Electrochemistry 67 (1992) 2.
[4] Ch. Zhi, Sens, et all., Lett 3 (2005) 274-295.
[5] R. Liu, et all., Sci Rep 7 (2017) 9761.
[6] P. Malinský, et all., Phys Stat Sol 256 (2018) 1800409.
[7] P. Malinský, et all., Surf Coatings Tech 342 (2018) 220–225.

Investigating pore evolution in Li & Li-CNT composite anodes

Neutron Physics Laboratory - Neutron diffraction

Neelima Paul

Proposal ID

539

Proposal # 539: Investigating pore evolution in Li & Li-CNT composite anodes

Sample description: Sample FGA, FGB, FGC and FGD are pouch bags containing Li pristine, Li cycled, Li-CNT pristine and Li-CNT cycled thin films, respectively. CNT is a short form for carbon nanotubes. We have an empty pouch bag (sample FG0) for background subtraction and a bag with pure CNTs (Sample FG1)

Instrument set-up: USANS measurements were conducted at MAUD facility – double bent crystals SANS installed at LVR-15 reactor in Rez near Prague. The samples were installed perpendicular to the incident neutron beam as shown in Fig. 1 and measured at three instrumental resolutions (high, medium and low) to cover a Q range from 0.01 to 0.0001 $Å^{-1}$. This should ideally allow investigations of lateral structures in the size range 20 nm - 2 µm. The neutron beam was focused on the sample center and the beam footprint on the sample was 15x4 mm^2. As the scattering was quite weak, each sample was measured about 24 hours in Dec 2021.

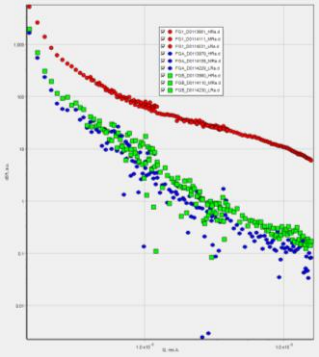

Fig. 1. USANS data of samples FG1, FGA, FGB (background subtracted using FG0)

Results: We wanted to gain information on pore evolution within these Li containing thin films upon cycling over the entire sample volume on the nano- and microscale with VSANS at MAUD. The USANS data shows that porous CNT powder sample (FG1) scatters the most due to higher contrast between CNT and air. The cycled Li sample FGB scatters slightly more than pristine Li sample FGA, which can be attributed to increased volume fraction of scatterers (eg. pores) , but it could also be due to difference in thicknesses between the two samples. The SANS curves from pristine Li-CNT sample FGC and cycled Li-CNT sample FGD appear same.

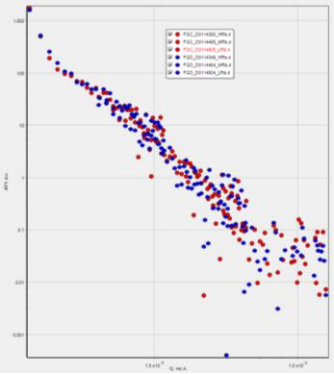

Fig. 2. USANS data of samples FGC, FGD (background subtracted using FG0)

Study of self-assembling effects in plasmonic metal-fullerene mixture films

Laboratory of Tandetron

Vasyl Lavrentiev

Proposal ID

476

Study of self-assembly effects in plasmonic metal-fullerene mixture films

Vasily Lavrentiev

Nuclear Physics Institute AS CR, Rez-130, Husinec 250 68, Czech Republic

In this study, I focused on identification of correlations between metal concentration, x, and surface nanostructure in the self-assembled Au_xC_{60}, Ag_xC_{60} and Cu_xC_{60} nanocomposite (NC) systems fabricated by simultaneous deposition of metal (Au, Ag or Cu) and C_{60} fullerene from vapour [1]. The main results of the study can be reported as the following. 1). RBS analysis does not show existence of oxygen in the Au_xC_{60} and Ag_xC_{60} NC films at any metal concentration, x. Contrary, significant amount of oxygen has been found in the Cu_xC_{60} films that evidences oxidation of the Cu nanoparticles (NPs) formed in the NC films during deposition (see the RBS spectra in Fig. 1). The oxygen concentration, y, gradually increases with x in the $Cu_xO_yC_{60}$ films reflecting growing NP surface fraction (see Fig. 1). 2). AFM study revealed a granular-like structure of the NC film surface (see AFM images in Fig. 1). Size of the granules is clearly varied with x suggesting the effect of metal-C_{60} chemical coupling. Thus, the increase of x in rather dilute films (approximately, with $x<1$) results in some decrease of the granule size. 3). The increase of x also causes non-monotonic variation of the film surface roughness (SR). In the dilute films of Au_xC_{60} and Ag_xC_{60} (with $x<1$), the increase of x results in jump of SR at some critical value of $x=x_{c1}$ ($x_{c1}\approx 1\div 2$, see Fig.1 and [1]) that is caused by formation of enlarged NPs on the film surface. Farther increase of x results in significant surface smoothing and decrease of SR (see Fig.1, in the right). Above $x \approx 15 \div 20$, SR rapidly increases in these films. The variations of SR with x indicate nucleation and growth of the metal NPs in the hybrid films [1]. 4). Interestingly, the increase of x at lower x ($x<1$) in the $Cu_x(O_y)C_{60}$ films results in rapid decrease of SR (see Fig. 1). At higher x ($x>1$), SR gradually increases in these films. Considering RBS results, one can relate such a SR behaviour with oxidation of the Cu NPs growing with x in the NC films. The obtained results will be published in relevant international journals. Some results are reported already in the references listed below.

References.

1. V. Lavrentiev, M. Motylenko, M. Barchuk, C. Schimpf, I. Lavrentieva, J. Pokorny, C. Röder, J. Vacik, A. Dejneka, D. Rafaja. Structure Assembly Regularities in Vapour-Deposited Gold–Fullerene Mixture Films, *Nanoscale Adv*. 2020, **2**, 1542-1550.
2. V. Lavrentiev, D. Chvostova, J. Pokorny, I. Lavrentieva, J. Vacik and A. Dejneka, Interplay of plasmonic and molecule excitations in self-assembled silver-fullerene nanocomposites, *Nanoscale* 2021 (submitted).

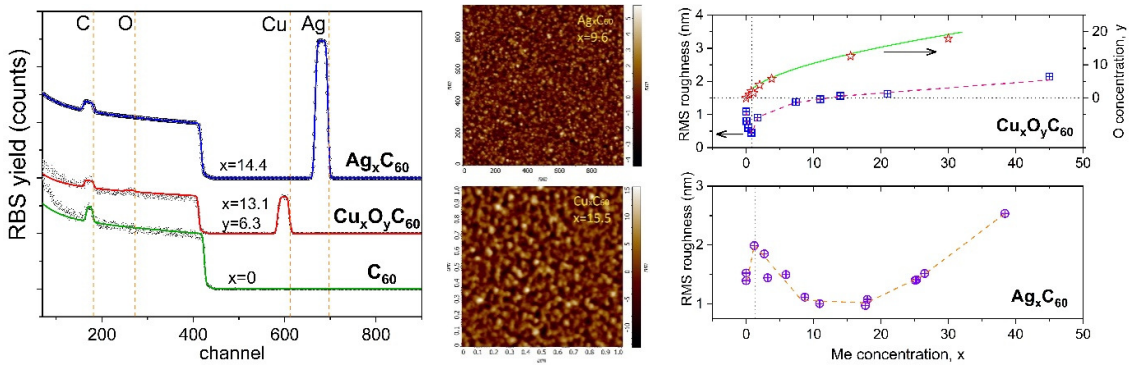

Figure 1: (*in the left*) Typical RBS spectra of the self-assembled Ag_xC_{60} and Cu_xC_{60} films shown for specific metal concentrations, x. RBS spectrum of pure C_{60} film ($x=0$) is also presented for comparison. Experimental and simulated spectra are shown by open dots and coloured curves, respectively. Vertical dotted lines indicate spectral position of the relevant elements located at the sample surface. (*in the middle*) Typical AFM images of Ag_xC_{60} (upper image) and Cu_xC_{60} films (lower image). (*in the right*) SR of the film surface as function of x shown for Cu_xC_{60} films (upper frame) and for Ag_xC_{60} films (lower frame). The upper frame also demonstrates dependence of oxygen concentration on x that is essential for Cu_xC_{60} films (stars, green curve).

Ion channelling effect and damage accumulation in yttria-stabilized zirconia implanted with Ag ions

Laboratory of Tandetron

Romana Mikšová

Proposal ID

477

Report regarding proposal "Ion channelling effect and damage accumulation in yttria-stabilized zirconia implanted with Ag ions."

R. Mikšová, A. Macková, A. Jagerová, P. Malinský, Nuclear Physics Institute of the CAS, v. v. i., Řež, Czech Republic
P. Harcuba, J. Veselý, Department of Physics of Materials, Faculty of Mathematics and Physics, Charles University, Czech Republic
V. Holý, Department of Condensed Matter Physics, Faculty of Mathematics and Physics, Charles University, Czech Republic
CEITEC at Masaryk University, Brno, Czech Republic
Institute of Ion Beam Physics and Materials Research, Helmholtz Zentrum Dresden-Rossendorf, 01328, Dresden, Germany

YSZ crystals were implanted with 400-keV Ag^+ ions over a broad fluence range at RT in three main crystallographic directions (100, 110, 111). This work aimed to investigate the relationship between the surface crystallographic orientation and the subsurface damage induced by Ag^+-ion implantation.

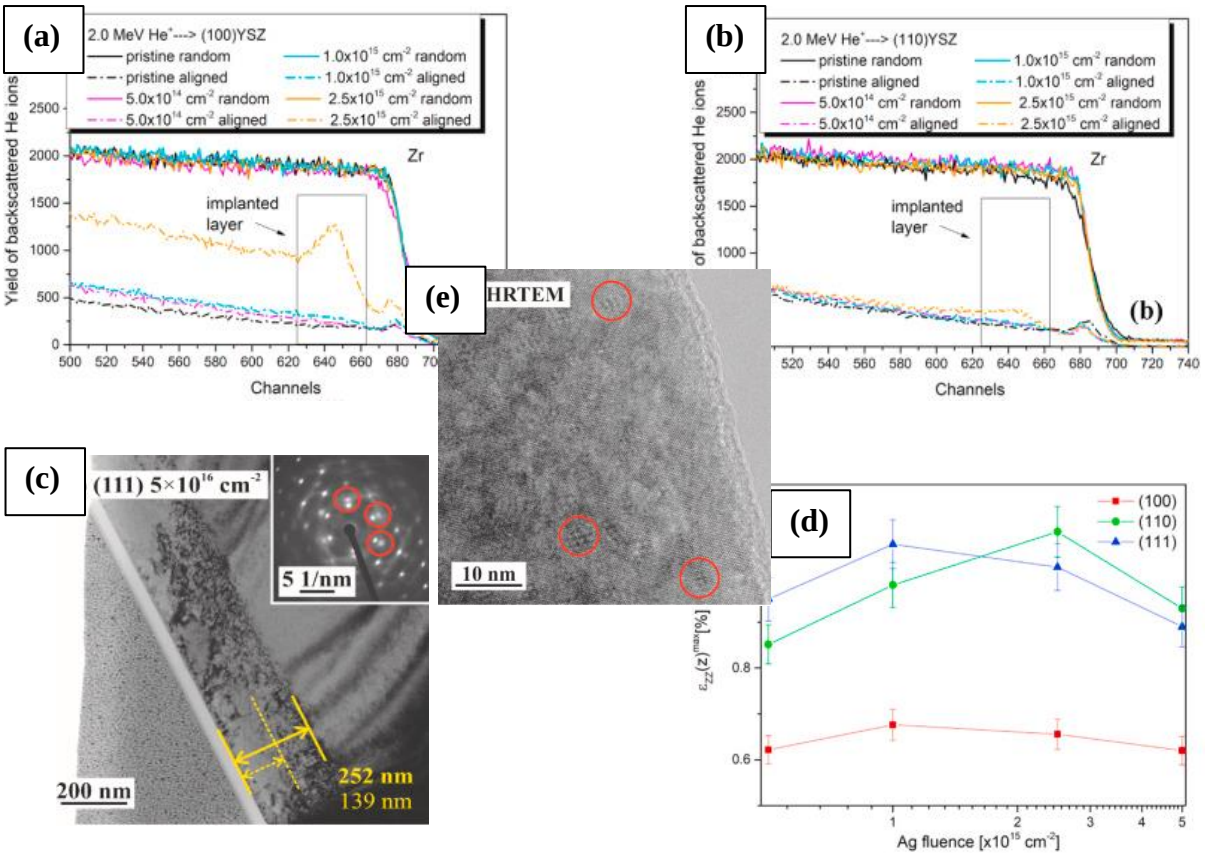

The full amorphisation of YSZ may not be possible under 400-keV Ag^+ irradiation at the ion fluences from 5×10^{14} to 5×10^{16} cm^{-2} at RT irrespective of crystallographic orientation. RBS-C measurements have revealed that the crystalline lattice of YSZ has been damaged but remains crystalline, which has been confirmed by TEM. RBS-C has shown that (110)-oriented YSZ is more radiation-tolerant than (100)- and (111)-oriented YSZ and the damage level f_{max} is below 0.3 (see Figure (a) and (b)).The damaged layer expands deeper in (110)-oriented YSZ than in the other two YSZ orientations; at the fluence of 5×10^{16} cm^{-2}, however, we already observed significant deepening of the damaged layer, comparable in all YSZ orientations (Figure (c)). XRD has characterised the structural damage in a broad range of fluences, where the tensile strain first increased and then relaxed (Figure (d)). The formation of Ag NPs is independent of the crystallographic orientations, which has been shown in TEM, and it is observed for the highest Ag-ion fluence used in the experiments (Figure (e)).

The results were published in NIMB a VACUUM.

Correlating the structure with Li conductivity in Ga and Al-doped LLZO electrolytes

Neutron Physics Laboratory - Neutron diffraction

Neelima Paul

Proposal ID

542

Proposal ID: #542

Title: Correlating the structure with Li conductivity in Ga and Al-doped LLZO electrolytes

Main proposer: Neelima Paul, TUM Garching, Germany

Instrument & Responsible: MEREDIT, Charles Hervoches

Goal: Both Ga and Al are used as dopants to enhance Li conductivity in LLZO electrolytes. However, it is unclear why Li conductivity is very high in Ga-doped LLZO, whereas it is quite low in Al-doped LLZO. We would like to gain insight on these lithium-ion migration mechanisms by refining the neutron diffraction data to correlate the conductivity with the structure. Additionally, we would like to obtain neutron diffraction data of doped LLZOs after their reaction with Li metal to correlate high Ga conductivity with Li reactivity and ultimately cycling performance of Ga-doped LLZO.

Technical details: We measured four samples for about 1 day each: (1) Li7–3*x*Al*x*La3Zr2O12 powder with x=0.2, (2) Li7–3*x*Ga*x*La3Zr2O12 powder with x=0.2, (3) Li7–3*x*Al*x*La3Zr2O12 pellet with x=0.2 and reacted with Li foil , (4) Li7–3*x*Ga*x*La3Zr2O12 pellet with x=0.2, and reacted with Li foil. The samples were filled in vanadium crucibles just before the measurement and sealed, and thus had a limited air exposure of 1 day (i.e. during measurement).

Results: In general, the statistics are not good, which can be both due to sample and the technique limitations. Rietveld refinements are used to identify the space group and extract lattice parameters for each sample. Al doped LLZO is seen to form a single garnet phase with SG cubic Ia_3d, whereas Ga doped LLZO is seen to form a single garnet phase with SG cubic I_43d with our sample composition. After exposure to air, Li – H exchange can cause slight increase of lattice parameters and appearance of shoulders on lower angle of Bragg peaks. LiCO3 formation can also cause an impurity peak. The Al doped LLZO seems not to change much after Li treatment whereas Ga doped LLZO undergoes a structural transformation to form a single garnet phase SG tetragonal I41/acd after Li treatment. A diffractogram from this sample (and the corresponding fit) is shown in Fig. 1.

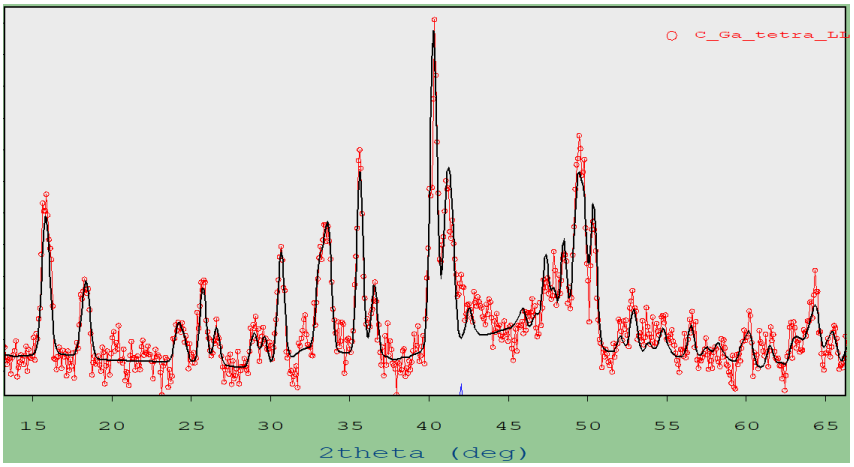

Fig. 1: Neutron diffractogram over a selected angular range for sample 4 (Li treated Ga doped LLZO).

Use of Polycarbonate for radiochromic dosimetry of proton and deuteron beams

Laboratory of Cyclotron and Fast Neutron Generators

David Zoul

Proposal ID

543

Research report

From 29.11.2021 to 30.11.2021, a series of experimental irradiations of radiochromic integrating MAKROCLEAR dosimeters by proton and deuteron beams accelerated on a U-120M cyclotron was performed at the CANAM workplace.

These dosimeters have been developed in the CVŘ since 2016. It is a solid-state clear polymeric material that responds to irradiation by changes in its optical density. For small doses, these changes first occur in the near UV region of the spectrum, then propagate into the light region and for even higher doses pass into the infrared region of the spectrum.

Dosimeters prepared in the shape of blocks measuring 10 x 10 x 20 mm were placed with their longest dimension parallel to the axis of the hadron beam in a special aluminum holder, behind a 10 mm thick aluminum collimator and a 9 mm diameter aperture so that the proton beam axis passes through the center of the sample.

During irradiation, the hadron beam was simultaneously monitored by a Farmer ionization chamber connected to a UNIDOS electrometer calibrated in the absorbed dose, so that the absorbed dose in the sample could be read in real time. The samples were successively irradiated with 15.5 MeV and 34 MeV protons at doses of 500 Gy, 2,500 Gy, 5,000 Gy, 10,000 Gy, 15,000 Gy. The next day, irradiation with 17 MeV deuterons continued at doses of 5,000 Gy, 10,000 Gy, 15,000 Gy.

This was followed by scanning the irradiated dosimeters on an Epson Perfection 850-Pro transmission scanner, through a series of color filters transmitting light wavelengths 640 nm, 580 nm, 510 nm, 450 nm, and through white light with a mean wavelength of 550 nm. The scanning was performed perpendicular to the beam axis to obtain information about the beam dose profile, and along the beam axis to obtain information about the depth dose curve (so-called Bragg curve) of the respective type of radiation. Because the material of dosimeter has only an 8% higher density than the average density of the human body, the results obtained can also be applied to Bragg curves in hadronic therapy of oncological diseases.

The bitmaps obtained by scanning were subsequently freed of noise caused by microscopic dust particles and impurities, which, despite thorough cleaning, were able to adhere to the surface of the samples. Low-pass filter convolution (image integration) was used for this. The convolution kernel consisted of a 3 x 3 matrix.

By accurately measuring the size of each sample with a micrometer gauge and comparing it with the number of pixels, the size of one pixel was determined and thus the correct dimensional scale of individual elements in the image. This made it possible to easily construct graphs of the depth dose curves and dose profiles of the individual bundles used, in a dimensional scale corresponding to reality.

Optical density (vertical axis in the graphs) was determined as absorbance, ie the decimal logarithm of the ratio of the intensity of radiation incident on the sample (mean value of light intensity outside the sample area) and intensity of radiation transmitted by the sample, divided by the thickness of the darkkening area of samples exposed and scanned in different ways).

The results of analyzes performed so far only in white (polychromatic) light have shown that MAKROCLEAR dosimeters are excellent as cheap and easily available integrating dosimeters of protons and light nucleuses in the dose range up to about 10 kGy, where their response in white light is practically linear to dose (with detectability threshold of about 100 Gy). This is approximately 20 times less than was previously observed with the same dosimeters after exposure to gamma photons of cobalt 60. However, this corresponds to the LET ratio for the photons and protons of the energies used, indicating that MACROCLEAR dosimeters respond to the relative biological efficiency (RBE) of different types of radiation, not just the absorbed dose. The MAKROCLEAR dosimeters so directly measure an dose equivalent.

Influence of the forging process on the precipitation behavior in the nickel-based superalloys

Neutron Physics Laboratory - Neutron diffraction

Frank Kümmel

Proposal ID

545

Experimental Report: "Influence of the forging process on the precipitation behaviour in nickel-based superalloys"

F. Kümmel[1], M. Fritton[1], R. Gilles[1]
1) Technical University Munich, Heinz Maier-Leibnitz Zentrum

The evolution of the different phases with temperature and the microstructure after different heat treatments was already investigated for the newly developed VDM® Alloy 780 by the authors of this proposal applying neutron diffraction (ND) and scanning electron microscopy (SEM).[1,2] However, the influence of forging on the precipitation of γ´ remains elusive. To elucidate the effect of forging fully solutionized (1020°C / 1h / air-cooled + 1080°C / 1h / water quenched) VDM® Alloy 780 samples were prepared as follows:

1) + 1000 °C / 1.3h without or with 50% compression / furnace cooling 25 °C/min -> forging

2) + 975 °C / 6h / water quenched -> HT precipitation

3) +800 °C / 6h / air-cooled -> γ´ precipitation

This three-stage processing route mimics the final steps of industrial material processing, i.e. forging (1), HT phase precipitation (2) and hardening phase precipitation (3). To isolate the influence of the forging, each sample was additionally prepared identically without deformation. XRD and SEM investigations were already performed but these techniques probe the alloy locally, leading to limited particle statistics. Therefore ND experiments were performed using the MEREDIT instrument with identical samples to get real bulk information. First results are are shown in Fig. 1.

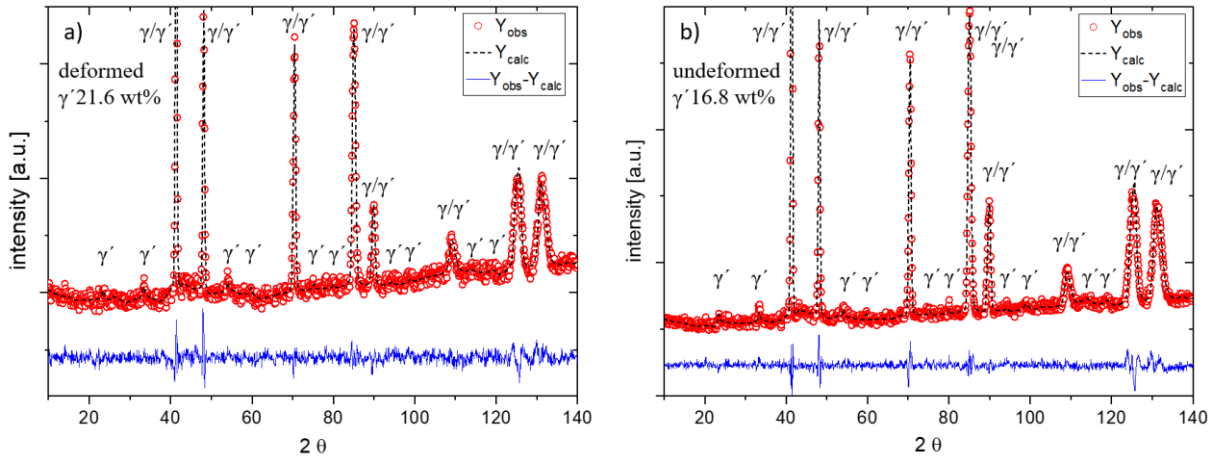

Fig. 1 Rietveld refinements of the VDM® Alloy 780 measured at room temperature (observed data (red circles), calculated data (black dotted line) and difference plot (blue line)) after the complete three-step processing route (1-3) a) for the deformed and b) for the undeformed specimen. The diffractograms were recorded at a wavelength of 1.46 Å.

The Rietveld refinements of condition 3 reveal γ´ phase fractions of 21.6 wt% and 16.8 wt% for the deformed and undeformed samples, respectively. This shows that, as expected, the forging process influences the precipitation process, which is evident from the approximately 5 wt.% higher proportion of γ'-phase in the deformed sample (cf. fig. 1 a).

1) C. Solís et al. in Metall. Mater. Trans. A (2018), 49, 4373–4381.

2) C. Solís et al. in Characterization of Minerals, Metals, and Materials (2019), 23–32

Study of elemental composition of volcanic ashes for geopolymer applications

Laboratory of Tandetron

Giovanni Ceccio

Proposal ID

546

Report - Proposal 546 “Study of elemental composition of volcanic ashes for geopolymer applications”

The project was focused on the determination of elemental composition of several volcanic ashes by nuclear analytical techniques such as RBS and Ion Microprobe-IBA using MeV ions (from Tandetron accelerator).

a) b)

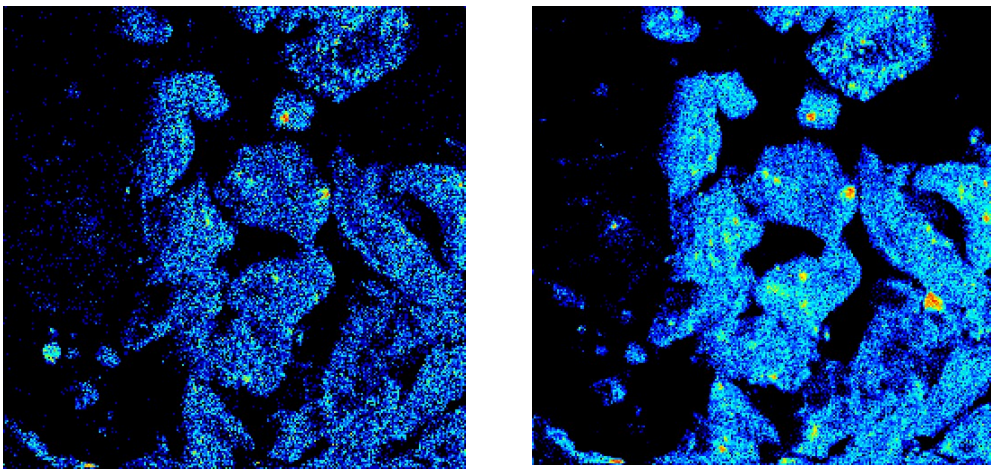

c) d)

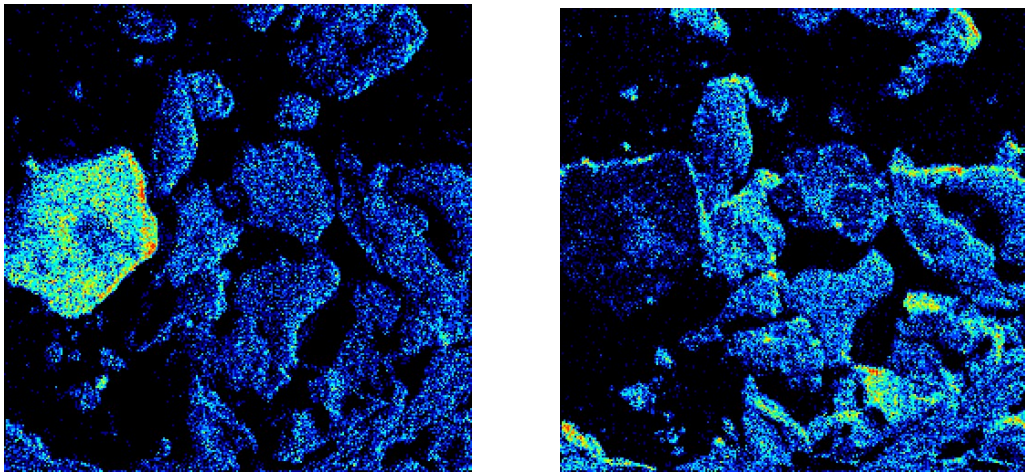

Microbeam analysis of volcano ashes, elemental investigation of: a) Ti, b) Fe, c) Si and d) Al

The obtained data are currently under evaluation and the comparison with complementary techniques suggests the possibility to have small traces of particular elements suitable for the preparation of geopolymers. The results are suitable for future publications when the data evaluation will be completed.

Investigation of deformation mechanisms in textured magnesium alloy

Neutron Physics Laboratory - Neutron diffraction

Jan Dittrich

Proposal ID

484

Report regarding proposal "Investigation of deformation mechanisms in textured magnesium alloy"

Due to its hexagonal close-packed lattice the deformation behavior of magnesium and its alloys is rather complex. There are several possible deformation mechanisms – slip systems are basal slip $(0001)\langle 11\bar{2}0\rangle$, prismatic slip $\{10\bar{1}0\}\langle 11\bar{2}0\rangle$ and second order pyramidal slip $\{11\bar{2}2\}\langle 11\bar{2}3\rangle$; other possibility is activation of deformation twinning, namely extension twinning $\{10\bar{1}2\}\langle 10\bar{1}0\rangle$, compression twinning $\{10\bar{1}1\}\langle 10\bar{1}2\rangle$ or double twinning $\{10\bar{1}1\}-\{10\bar{1}2\}$ [1]. In order to meet the Von Mises criterion [2] and achieve homogenous plastic deformation a mechanism providing elongation along the <c> axis, typically the extension twinning or the second order pyramidal slip, needs to be activated. The activation of any given deformation mechanism is strongly dependent on the alloying elements, temperature and the combination of texture and loading direction – the last of which was investigated in this study.

The AZ31 magnesium alloy used in this study exhibited a typical texture of wrought alloys, i. e. basal texture in the normal plane of the sheet (Fig 1). The effect of texture on activity of the individual deformation mechanisms (following the Schmid law [3]) can be examined by deformation of samples machined in various directions with regards to the sheet texture in such way that they are preferentially oriented for different deformation mechanisms. Four orientations were selected – RD (rolling direction), ND (normal direction), 45 (direction at 45° between RD and ND) and 30 (direction at 30° between rolling direction and transversal direction).

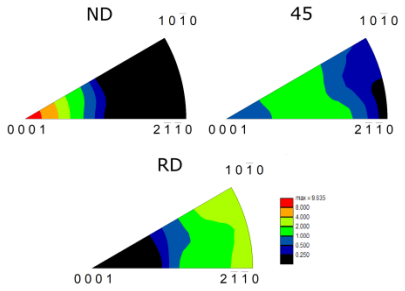

Figure 1 Inverse pole figure (IPF) of the ND, 45 and RD oriented samples.

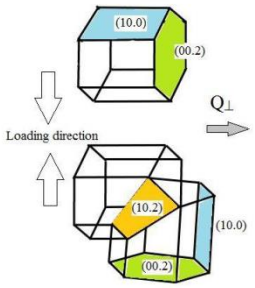

Figure 2 Extension twinning$\{10\bar{1}2\}\langle 10\bar{1}0\rangle$ in compression [4]

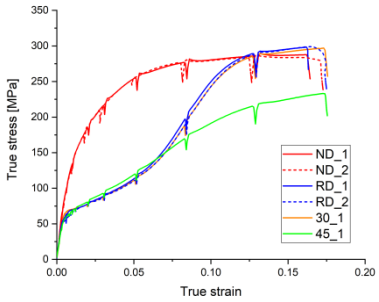

Figure 3 True stress – true strain deformation curves

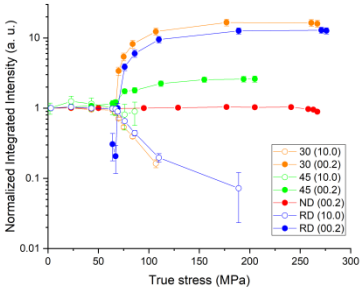

Figure 4 Normalized integrated intensities of the $(10\bar{1}0)$ and (0002) diffraction peak

The extension twinning$\{10\bar{1}2\}\langle 10\bar{1}0\rangle$, being the preferred deformation mechanism for the compressive deformation of the RD and 30 samples, is accompanied by rapid reorientation of the twin by 86,3° with regards to the parent grain (Fig. 2). This is accompanied by shift of diffracted intensity from the $(10\bar{1}0)$ plane to the (0002) plane and can be thus evaluated based on the measured neutron diffraction spectra. A supplementary recording of the acoustic emission signal during loading of the samples provides further and complementary information about the activity of the individual deformation mechanisms.

Neutron diffraction spectra were measured on samples of all above mentioned orientations using the two-axis diffractometer TKSN-400. The samples were strained up to fracture and the experiment was interrupted at 3 points in the elastic part and at selected values of strain in the plastic region (0.5, 1, 2, 3, 5, 8, 12 and 15%) in order to collect the diffraction data (Fig 3).

The $(10\bar{1}0)$ to (0002) peak intensity shift was very significant in the RD and 30 samples, confirming major role of extension twinning particularly in the early stages of plastic deformation. No major differences between these orientations in terms of twinning activity was observed leading to the conclusion that the angle of rotation around the ND direction does not seem to have major influence on mechanical twinning. The 45 sample (oriented favorably for basal slip) also exhibits a certain level of twinning activity, though not as pronounced as the RD and 30 samples. There was no $(10\bar{1}0)$ – (0002) intensity shift observed in the ND sample indicating virtually no extension twinning activity during compressive deformation.

References

[1] Agnew, S. R. and Duygulu, O., 2005, Plastic anisotropy and the role of non-basal slip in magnesium alloy AZ31B, Int. J. Plast., 21 (6), pp 1161-1193
[2] Mises, R. von, 1928, Mechanik der plastichen formänderung von kristallen Zamm – Z., Angew. Math. Me., 8 (3), pp 161-185
[3] Schmid, E. and Boas, W., Plasticity of crystals with special reference to metals, F.A. Hughes, London, 1950.
[4] Máthis, K., Beran, P., Čapek, J. and Lukáš, P., 2012, In-situ neutron diffraction and acoustic emission investigation of twinning activity in magnesium, J. Phys. Conf. Ser., 340

Study of advanced silicon radiation detectors

Laboratory of Tandetron

Maria Marcisovska

Proposal ID

489

Report regarding proposal “Study of advanced silicon radiation detectors”

The conducted experiment was focused on two tasks:

I. Spectral and Angular Response of a Silicon Strip Detector Based on PH32 ASIC
M. Kaschner, P. Stanek, P. Svihra, FNSPE CTU in Prague

The primary focus of the first study is energy calibration of a silicon-strip detector used for alpha particle spectrometry. The energy range of alpha particles used for calibration was from 2 MeV up to 9 MeV. Secondary aim is to observe the effect of the incidence angle on the response of the device. The results will be used for future radionuclide identification and activity measurements.

For the purposes of the study, the detector was placed in a vacuum chamber on a motorized arm, which provides movement of the detector in and out of the particle beam, as well as changes of the angle of the incidence. The measurements required very low particle flux (lower than the minimal detection limit needed by the flux measuring device). In order to reduce the pile-up of the particles in the individual strips, the device was placed outside of the center of the beam which was then collimated to 5×0.2 mm^2. An example of the reproduced spectra is shown in Figure 1a, the dependency of ToT as a function of energy in Figure 1b. The effect of the angle of incidence variation on ToT is in Figure 1c.

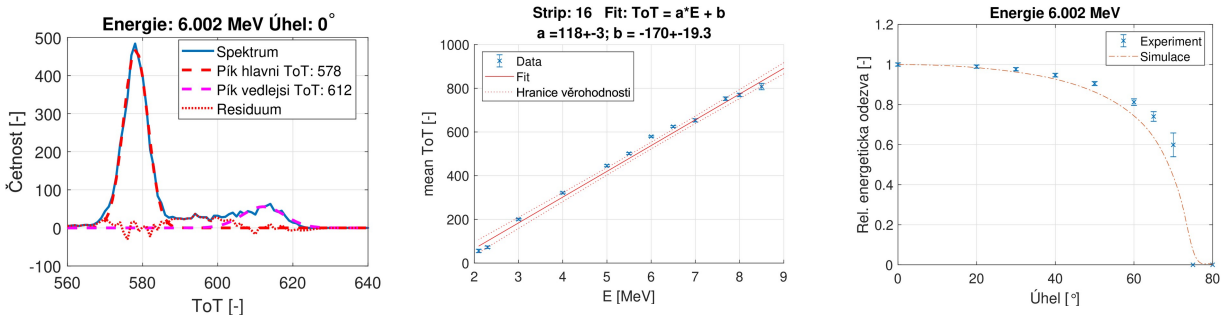

Figure 1: Measured dependencies. (a) Example of measured spectra and locations of visible peaks. (b) Observed dependence of detector response on the energy of alpha particles and its linear fit. (c) Observed dependence of detector response on angle of incidence of alpha particles and expected dependency according to simulations in SRIM.

II. Study of advanced monolithic silicon detectors using highly ionizing ions
M. Havranek, A. Kabatova, A. Kostina, M. Marcisovska, FNSPE CTU in Prague

The second task is aimed at the study of pixel matrix response of the SpacePix and X-CHIP monolithic detectors to different ions.

Protons with an energy of 6 MeV, helium nuclei with an energy of 8-9 MeV and lithium nuclei with an energy of 12 MeV were used for irradiation. The images recorded from the individual sensors were analyzed. Figure 2 shows the interactions of protons, helium nuclei and lithium in the SpacePix-2-Log sensor. The sensor can display individual interactions of all types of ions. Relatively small clusters were observed for all types of ions, rarely exceeding 2×2 pixels in size. Despite the relatively high deposited energies close to the saturation of the measuring channels, a clear difference in the amplitude of the signal from protons and He/Li can be seen. However, to distinguish He from Li, more advanced analysis techniques need to be used, which also take into account the size of the clusters.

The relatively low energy of ions leads to saturation of the sensors. To better understand the response of SpacePix sensors, it is necessary to use ion beams with higher energy in the order of hundreds of MeV, where the ions leave only part of their original energy in the sensitive layer of the sensor and, based on specific energy losses, to test the ability to identify different types of ions.

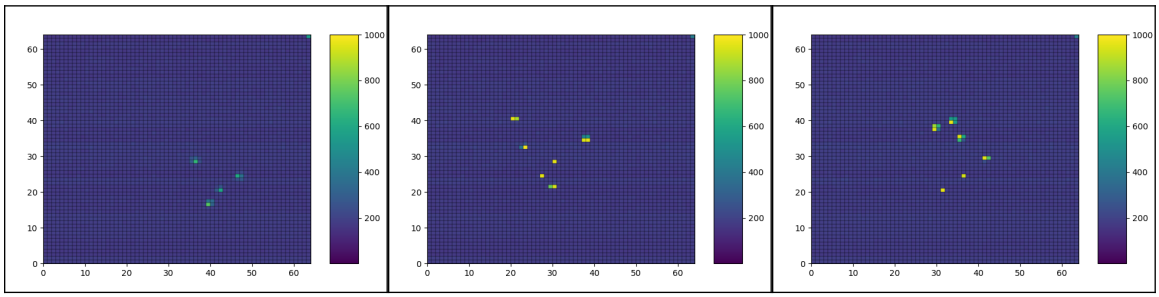

Figure 2: Interactions of protons (left), helium nuclei (middle) and lithium (right) in the SpacePix-2-Log sensor.

Nanostructuring of crystalline ZnO by energetic ion beams for optoelectronic applications

Laboratory of Tandetron

Adela Jagerova

Proposal ID

490

Report regarding proposal "Nanostructuring of crystalline ZnO by energetic ion beams for optoelectronic applications"

Adéla Jagerová[1,2], *Jan* Mistrík[3,4], and *Anna* Macková[1,2]
[1]Nuclear Physics Institute of the Czech Academy of Sciences, p.r.i, 250 68 Řež, Czech Republic
[2]Department of Physics, Faculty of Science, J.E. Purkyně University, Pasteurova 3544/1, 400 96 Ústí nad Labem, Czech Republic
[3]Institute of Applied Physics and Mathematics, Faculty of Chemical Technology, University of Pardubice, 532 10 Pardubice, Czech Republic
[4]Centre of Materials and Nanotechnologies, Faculty of Chemical Technology, University of Pardubice, 530 02 Pardubice, Czech Republic

The surfaces of *c*-, *a*- and *m-plane* ZnO were nano-structured using the 27 MeV W ion irradiation with ion fluences of 5×10^{9}, 5×10^{10} and 5×10^{11} cm^{-2}. RBS-C analysis revealed only low Zn-disorder up to the depth of 1.38 μm in all studied orientations (e.g. Figure 1a for *c-plane* ZnO). The irradiation-induced increase of surface roughness and formation of nano-hillocks on the *c*- and *a-plane* ZnO and huge moulds on the *m-plane* ZnO (Figure 1b and c for *c*- and *m-plane* ZnO, respectively).

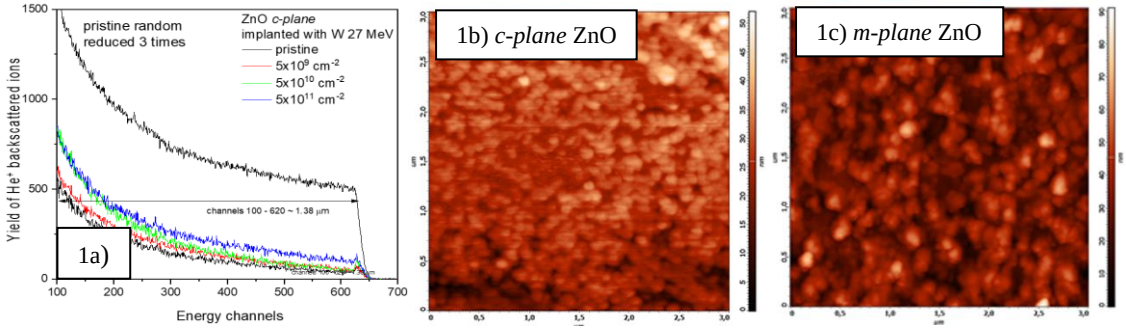

The crystalline ZnO nanopillars with a thickness of about 400 nm were modified with Au NPs prepared by 400 keV Au ion implantation with ion fluences of 1×10^{15}, 5×10^{15} and 1×10^{16} cm^{-2}. The growth of Au NPs was further supported with thermal annealing at 600 °C on air. The ion implantation decreases ZnO nanopillar thickness as observed by RBS (Figure 2a). The implanted Au ions modified the depth of about 250 nm. The higher implantation depth exhibited a shift of implanted Au ions towards the surface, see Figure 2b. The distribution of implanted Au ions did not significantly change after thermal annealing. The optical properties of implanted ZnO nanopillars, expressed by extinction coefficient, showed surfaced plasmon resonance (SPR) peak typical for Au NPs in a wavelength region of 400 – 800 nm, see Figure 2c. The SPR peak is shifted against a higher wavelength with increasing Au ion fluence indicating the creation of bigger Au NPs with higher fluence. SPR peak is further shifted towards a higher wavelength after thermal annealing due to the growth of Au NPs and the formation of bigger complex clusters.

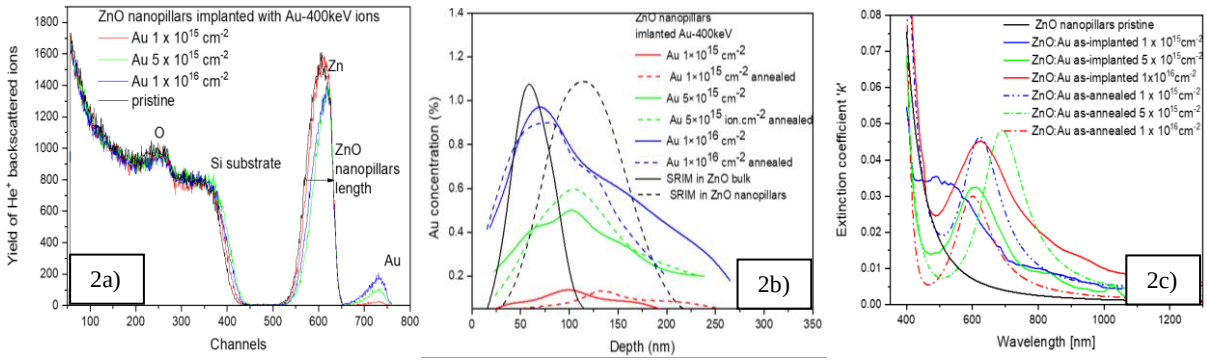

The results obtained for 27 MeV W irradiated *c*-, *a*- and *m-plane* ZnO surfaces were summarized and published in Physical Chemistry Chemical Physics journal. The modification of ZnO nanopillars with Au NPs prepared with 400 keV Au implantation was published in the Journal of Physics D: Applied Physics.

Microstructures in ethanol/water mixtures

Neutron Physics Laboratory - Neutron diffraction

Petr Stepanek

Proposal ID

497

Proposal ID 497

Title Microstructures in ethanol/water mixtures

A mixture of deuterated ethanol (90%) and water (10%) was prepared in 2mm quartz cells. For measurement of the background a cell filled with pure deuterated ethanol was used. Scattered intensity data were acquired with low, medium and high resolution. The scattered intensity was not too high, nevertheless the anticipated form factor of the scattering domains could be obtained. A typical result is shown in the following figure.

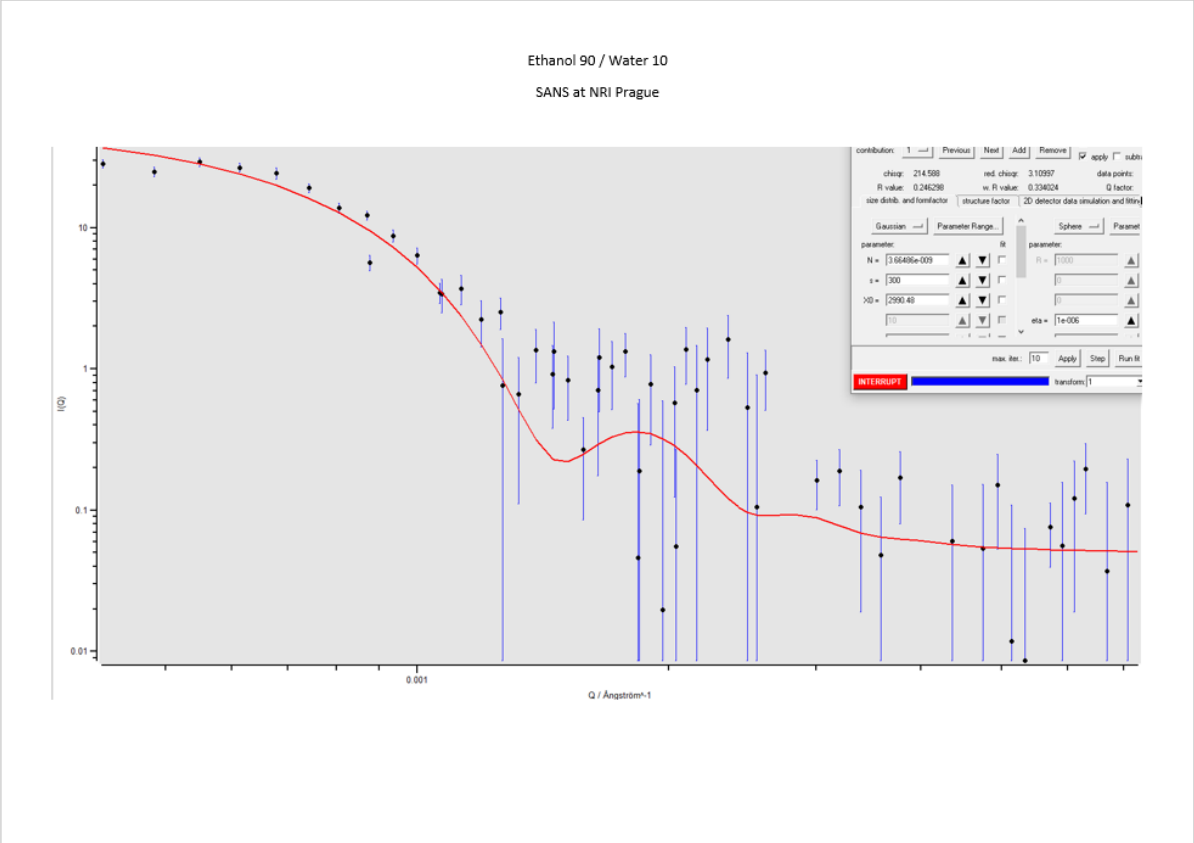

The scattering curve was fitted with a form factor of a homogeneous sphere with a Gaussian distribution of sizes, the mean size being 2990 A and distribution width 10 %.

This result is very valuable since it sets the geometrical scale of the microstructure for further investigations by various experimental techniques.

Quantitative in-situ analysis of nano-scale precipitates during ageing heat treatment of additively

Neutron Physics Laboratory - Neutron diffraction

Ahmad Kermanpur

Proposal ID

506

Quantitative in-situ analysis of nano-scale precipitates during ageing heat treatment of additively manufactured IN718 Ni-based superalloy

Ahmad Kermanpur and Peter Hedström, KTH Royal Institute of Technology, Sweden
Vasyl Ryukhtin, Nuclear Physics Institute, Řež, Czech Republic

Temporal evolution of the nano-scale strengthening precipitates during double-stage ageing heat treatment of the laser powder-bed fusion (LPBF) additively manufactured IN718 Ni-based superalloy is studied by small-angle neutron scattering (SANS) experiments. The rectangular specimens ($10\times10\times2$ mm^3) were investigated both *ex-situ* at room temperature and *in-situ* using a vacuum furnace following the ageing treatment. The thermal cycle consisted of a solution treatment at 1060 °C for 1 h followed by a double-stage ageing at 760 °C for 10 h, furnace-cooling, and 650 °C for 8 h, followed by air-cooling. The desired instrumental resolution spanned a scattering vector (Q) range of $0.02<Q<0.2$ nm^{-1} at a constant incident neutron wavelength of 0.209 nm, corresponding to scattering features with sizes from about 30 nm up to 300 nm in real space. The *ex-situ* measurements of the wrought and LPBF IN718 superalloy samples were first carried out with full statistics for 3.5 h. The *in-situ* SANS were conducted during ageing treatment of solution treated samples with a 20 min acquisition repetition at low instrumental resolution. The raw data were treated by standard procedure using "empty furnace" and "cadmium" scattering corrections. A simple spherical model with log-normal size distribution was used for fitting of precipitates. The fitting was done using SASProFit software.

The *ex-situ* SANS data of the LPBF and wrought samples are shown in Fig. 1. The observed increase of the SANS intensity in the aged samples compared to the solution treated ones, is caused by nucleation and growth of the nano-scale γ′′ (Ni_3Nb) and γ′ (Ni_3Al) precipitates. Neutron scattering length densities (SLD) of the γ′ and γ′′ phases as empirically calculated using compositions of TC-PRISMA simulations are very close (*i.e.* $SLD^{\gamma'}= 7.5177\times10^{10}$ Å^{-2}, $SLD^{\gamma''}= 7.5388\times10^{10}$ Å^{-2}). Therefore, these precipitates are practically indistinguishable by SANS. The differences in SANS scattering of the aged and solution treated samples in the high Q region were supposed to be caused by γ′′ and γ′ precipitates and therefore used for fitting using spherical models with log-normal size distribution. The fitted volume fraction of γ′′ and γ′ particles is higher for wrought (26.6 ± 0.19 %) than for LPBF (10 ± 3.5 %) alloy. However, these results are distorted by the instrumental limitation of the highest measured angle $Q_{max} \approx 0.2$ nm^{-1} which corresponds in real space to a minimum size which is possible to detect of $R_{min} \approx 15$ nm. Nevertheless, in the given windows, the wrought material after heat treatment contains more than twice higher particle volume fraction than the aged LPBF alloy. In fact, growth rate of the γ′′ precipitates is faster in the wrought material than in the LPBF one. The SANS data from the solution treated LPBF is higher than for the corresponding wrought one, obviously due to higher population of scattering particles like MC carbides and Laves phases.

Total counts of *in-situ* SANS raw data in dependence on ageing time are shown in Fig. 2. Monotonic increasing of scattering at 760 °C is caused by nucleation and growth of the precipitates and corresponds to increasing of their volume fraction in the covered size range. Interestingly, SANS total counts within statistical error remain constant during the second stage of ageing (at 650 °C during 10-18 h) due to stable volume fraction.

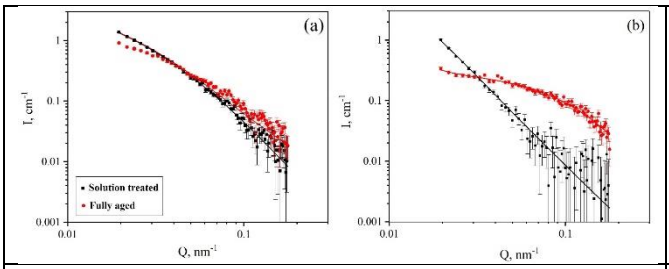

Fig. 1. *Ex-situ* SANS data for the (a) LPBF and (b) wrought samples in both solution treated and aged conditions.

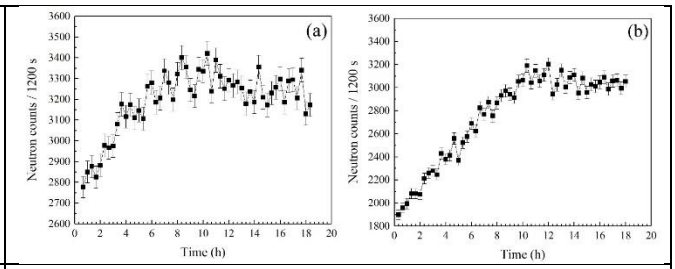

Fig. 2. *In-situ* SANS raw data during ageing treatment of the (a) LPBF and (b) wrought samples.

The *ex-situ* SANS data showed that the growth rate of the nano-scale precipitates is faster in the wrought material than in the LPBF one. The *in-situ* SANS data showed that the volume fraction of the nano-scale precipitates monotonically increases during the first stage of ageing and stagnates during the second stage. This information, which has not been reported before, suggests that a shorter ageing treatment compared to the standard cycle presented for the conventional alloy might be applicable for ageing the LPBF IN718 superalloy.

Neutron Diffraction of solid electrolyte materials for joint XRD/ND refinement

Neutron Physics Laboratory - Neutron diffraction

Stefan Seidlmayer

Proposal ID

508

Report regarding proposal "Neutron Diffraction of solid electrolyte materials for joint XRD/ND refinement"

S. Seidlmayer, I. Pivarnikova, T. Pham, R. Gilles, MLZ (Heinz Maier-Leibnitz Zentrum, Technical University Munich, Germany), C. Hervoches, Nucl. Physics Inst., Rez, Czech Republic

Five different samples and an empty sample container for background correction were measured at the MEREDIT instrument. The data were obtained at 298 K with a mosaic copper crystal monochromator, with the Cu(220)-reflection giving a wavelength of 1.46 Å. Two different solid electrolyte materials [1] for future lithium or sodium ion batteries were studied. One sample of Ta-doped and undoped LLZ ($Li_7La_3Zr_2O_{12}$) solid-electrolyte materials [2, 3] and two datasets of NASICON based ($Na_{1+x}Zr_2Si_xP_{3-x}O_{12}$ ($0 \leq x \leq 3$) solid electrolytes [4, 5] were obtained measuring the scan range between 4 and 140 °2Θ with a step size of 0.1 °2Θ and a total counting time of 24h45min per sample. Additionally, one sample of cathode material for lithium ion batteries (NCA, $LiNi_{0.8}Co_{0.15}Al_{0.05}O_2$) was gathered for 12h22min. The data analysis of the solid electrolyte materials is still in progress and not finished at this time. We thus want to report on the results of the NCA-data set with a nominal composition of $LiNi_{0.8}Co_{0.15}Al_{0.05}O_2$. The crystal structure of this material is reported to be a layered oxide with the spacegroup R -3 m (No. 166). The oxygen atoms on the position 6c (0, 0, 0.25857(33) form a cubic close packing, the metal ions Ni, Co and Al occupy octahedral voids on position 3a on (0, 0, 0) and Li ions octahedral voids in 3b (0, 0, ½). The refinement of the neutron data (see fig. 1) confirms this arrangement and the lattice parameters are a = 2.8648(1) Å and c= 14.1852(9) Å. One important structural detail for the application in lithium ion batteries is the amount of oxygen vacancies and Li/Ni site mixing – both parameters influence the electrochemical behaviour, or change upon battery degradation. In addition, we have obtained XRD data on the same material and the obtained values for the oxygen vacancies and especially on the Li/Ni site mixing appeared to be very different from the expectations. The neutron data now give a much better result. Later, we want to combine both data sets for a joint-refinement approach in order to combine the strength of both methods, while compensating for the weaknesses. The data were refined using the provided instrument resolution file. First, the background was approximated with the Sonneveld&Visser algorithm [6] in the Highscore software v4.9 [7] using 300 points for the background interpolation, which were then imported to Fullprof v7.30 [8] for the neutron refinement. The data refinement proceeded with Thompson-Cox-Hastings profiles including an asymmetry treatment according to Finger-Cox-Jephcoat. Refined site mixing and oxygen content results from both XRD and ND data and the expectation values from the materials specification sheet are summarized in the table below.

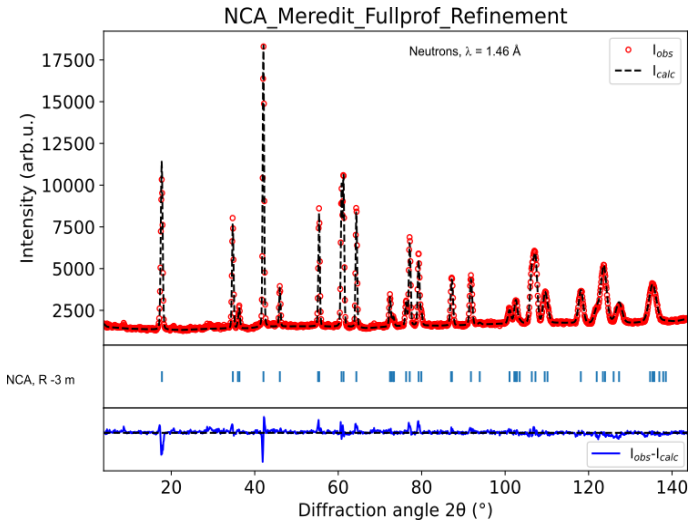

Fig. 1: Data & refinement of $LiNi_{0.8}Co_{0.15}Al_{0.05}O_2$ with R -3 m structure

Refinement-type	Li/Ni mixing	Oxygen content	R-values
Material specification	0.05	1.985	-
XRD	0.012	1.876	R_{Bragg} = 5.68 %; R_{wp} = 12.76 %
ND	0.037	1.926	R_{Bragg} = 7.24 %; R_{wp} = 12.20 %

References

1. He, X., Bai, Q., Liu, Y., Nolan, A. M., Ling, C. and Mo, Y., 2019, Advanced Energy Materials, 9(43), 1902078.
2. Thompson, T., Sharafi, A., Johannes, M. D., Huq, A., Allen, J. L., Wolfenstine, J. and Sakamoto, J., 2015, Advanced Energy Materials, 5(11).
3. Mukhopadhyay, S., Thompson, T., Sakamoto, J., Huq, A., Wolfenstine, J., Allen, J. L., Bernstein, N., Stewart, D. A. and Johannes, M. D., 2015, Chemistry of Materials, 27(10), 3658-3665.
4. Goodenough, J. B., Hong, H. Y. P. and Kafalas, J. A., 1976, Materials Research Bulletin, 11(2), 203-220.
5. Hong, H. Y. P., 1976, Materials Research Bulletin, 11(2), 173-182.
6. Sonneveld, E. J. and Visser, J. W., 1975, Journal of Applied Crystallography, 8, 1-7.
7. Degen, T., Sadki, M., Bron, E., Konig, U. and Nenert, G., 2014, Powder Diffraction, 29, S13-S18.
8. Rodriguez-Carvajal, J., 1993, Physica B: Condensed Matter, 192(1–2), 55-69.

Study of structural properties of MAX/MX phase thin films synthetized by ion beam sputtering

Laboratory of Tandetron

Giovanni Ceccio

Proposal ID

445

Report regarding the proposal "Study of structural properties of MAX/MX phase thin films synthetized by ion beam sputtering"

G. Ceccio, P. Horak, A. Cannavò

Nucl. Physics Inst., Rez, Czech Republic

MAX phases are ternary carbides or nitrides with the formal stoichiometry formula of Mn+1AXn (n = 1, 2, 3), where M is representative of an early-transition d metal (i.e., Sc, Ti, V, Cr, Zr, Nb, Mo, Hf, and Ta), A is an element from (mainly) the IIIA or IVA group (i.e., Al, Si, P, S, In, Sn, and Pb), and X is either carbon or nitrogen. The properties of the MAX and MXene systems are based on combination of the best attributes of the metals and ceramics. For example, MAX phases are resistant to radiation, thermal shock or corrosion and exhibit high electrical conductivity. Thin films of MAX and MXene phases were prepared by ion beam sputtering followed by thermal annealing in vacuum. The thickness, composition and stoichiometry of the films were analyzed by the Rutherford Back-scattering method (RBS) and Nuclear Resonance Analysis (NRA) using α-particles with an energy of 2000 keV and 3.046, 4.280 keV for RBS and NRA, respectively. The measurements were carried out at the Tandetron 4230 MC accelerator at NPI (CANAM infrastructures). Important results were obtained studied the MAX phases: Ti_3InC_2 and Ti_2SnC (see Fig. 1)

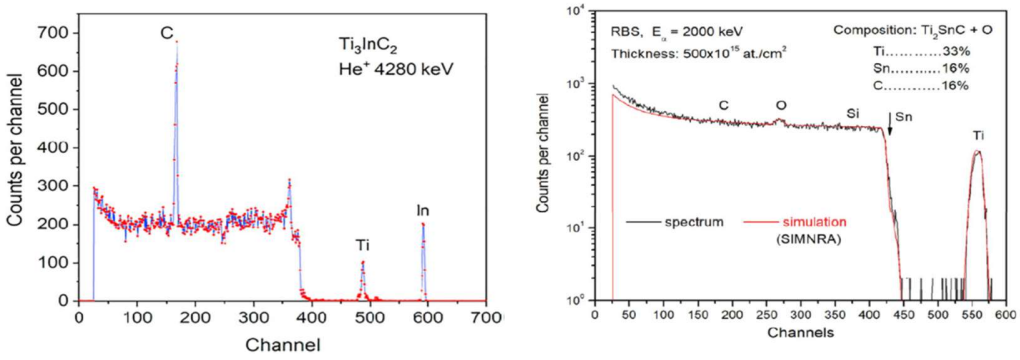

Figure 1 The NRA spectra of the Ti3InC2 film showing the C resonance analysis at 4280 keV(left) IBA analysis of the Ti2SnC thin film: RBS using 2 MeV alpha particles (right)

The data concerning the preparation of the MAX phase thin films by ion sputtering were partially published [1,2], but other results concerning the modification of the thin films by ion implantation are still under evaluation for future publications.

[1] Surface and Coatings Technology Volume 394, 25 July 2020, 12583
[2] RADIATION EFFECTS & DEFECTS IN SOLIDS 2020, VOL. 175, NOS. 1–2, 177–189

Excitation functions of the of proton- and deuteron-induced reactions on Zn-64, As-75, Y-89, Mo-100

Laboratory of Cyclotron and Fast Neutron Generators

Ondrej Lebeda

Proposal ID

64

Excitation functions of the of proton- and deuteron-induced reactions on ^{64}Zn, ^{75}As, ^{89}Y, ^{100}Mo

Ondřej Lebeda, Vlasta Zdychová, Jaroslav Červenák and Jan Štursa

Nuclear Physics Institute, Řež, Czech Republic
Czech Technical University, Prague

Detailed measurement of the deuteron-induced excitation functions on ^{89}Y in the energy range of 3.9–19.5 MeV was performed resulting in new excitation function for formation of ^{88}Zr, ^{89m}Zr, ^{89}Zr, ^{88}Y, ^{90m}Y and ^{87m}Sr (Fig. 1). The data were compared with previously published results and prediction of the TALYS code. Parallel use of titanium and aluminium beam monitors revealed systematic difference between the recommended cross-sections of both monitoring reactions and provided new cross-section data for formation of ^{24}Na, ^{27}Mg, ^{43}Sc, ^{44m}Sc, ^{44}Sc, ^{46}Sc, ^{47}Sc and ^{48}Sc (Fig. 1). Results were published in a peer-reviewed journal [1] and included in the EXFOR data base.

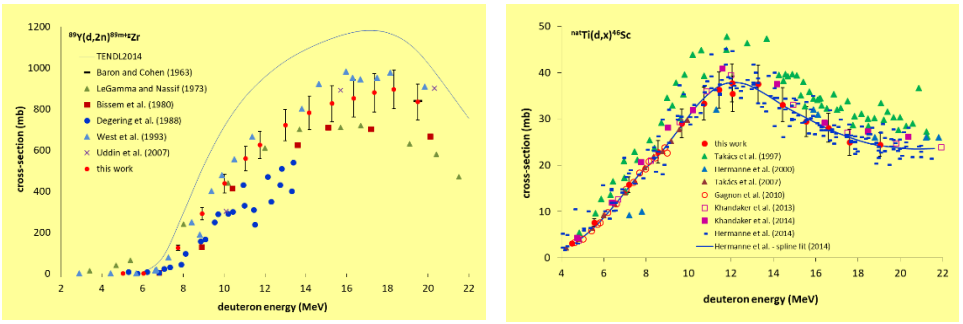

Fig. 1 Excitation function of the ^{89}Y(d,2n)$^{89m+g}$Zr for the formation of medically relevant ^{89}Zr amd excitation function of the ^{nat}Ti(d,x)^{46}Sc suitable for the beam monitoring

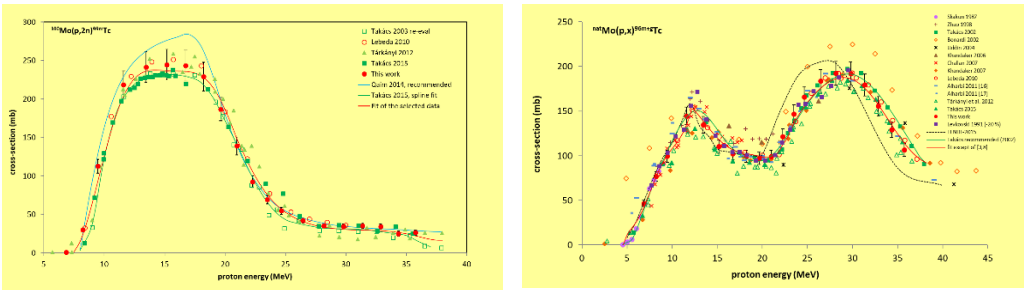

Fig. 2 Selected cross-sections for the ^{100}Mo(p,2n) nuclear reaction and fit of the recommended values; cross-sections for the beam monitoring reaction ^{nat}Mo(p,x)$^{96m+g}$Tc and their fitting resulting in the recommended data

Due to the lack of thin foils of precise thickness made out of highly enriched metals, we decided to re-measure excitation functions of protons on natural molybdenum, as the elemental cross-sections may be in the case of the nuclear reactions on ^{100}Mo converted into isotopic cross-sections. The extensive experiment allowed us then to provide another set of data important not only for the production of medically relevant ^{99m}Tc and ^{99}Mo, but also for the ^{nat}Mo(p,x)$^{96m+g}$Tc reaction relevant for both beam monitoring and TLA, as well as data for production of ^{95m}Tc, a suitable long-lived technetium tracer. Altogether, almost 30 excitation functions were obtained covering the proton beam energy range of 7–36 MeV, some of them were provided for the first time (^{97m}Tc, ^{88g}Nb, ^{88m}Nb and ^{89m}Nb) [2]. Results are included in the EXFOR data base.

Due to the problems with the target preparation, we have resigned on the measurement of the proton-induced excitation functions on ^{64}Zn. The sputtered targets made out of ^{75}As were not suitable for the proton beam activation, the bombardment resulted in their significant damage that didn't allow for obtaining reliable data.

The rich experimental material collected during the experiments was then included in an extensive works performed within the IAEA CRP project.

[1] Lebeda, O. – Štursa, J. – Ráliš, J. Experimental cross-sections of deuteron-induced reaction on ^{89}Y up to 20 MeV; comparison of ^{nat}Ti(d,x)^{48}V and ^{27}Al(d,x)^{24}Na monitor reactions. *Nuclear Instruments and Methods in Physics Research B*, 2015, vol. 360, pp. 118–128.
doi: 10.1016/j.nimb.2015.08.036

[2] Červenák, J. – Lebeda, O. Experimental cross-sections for proton-induced reaction on ^{nat}Mo. *Nuclear Instruments and Methods in Physics Research B*, 2016, vol. 380, pp. 32–49.
doi: 10.1016/j.nimb.2016.05.006

Structure determination of Ca3Ga2-2xZnxGe4+xO14

Neutron Physics Laboratory - Neutron diffraction

Mathieu ALLIX

Proposal ID

516

Report regarding proposal "Structure determination of $Ca_3Ga_{2-2x}Zn_xGe_{4+x}O_{14}$"

H. Bazzaoui, C. Genevois, M. Pitcher, M. Allix, CNRS, CEMHTI UPR3079, Univ. Orléans, F-45071, Orléans, France

P. Beran, Nucl. Physics Inst., Rez, Czech Republic

Using an original glass crystallisation approach, we have synthesised a new solid solution, namely Ca3Ga2-2xZnxGe4+xO14. Following our synchrotron powder diffraction (SPD) investigations, we have applied neutron powder diffraction data measurements on the MEREDIT diffractometer in order to clearly establish the structure of 3 different compositions this solid solution: Ca3Ga2Ge4O14 (x=0), Ca3GaZn0.5Ge4.5O14 (x=0.5) and Ca3ZnGe5O14 (x=1).

The extracted data is still under evaluation but preliminary results already show the precise occupation on the Ga/Zn/Ge mixed sites which could not be accessed by SPD (see figures below).

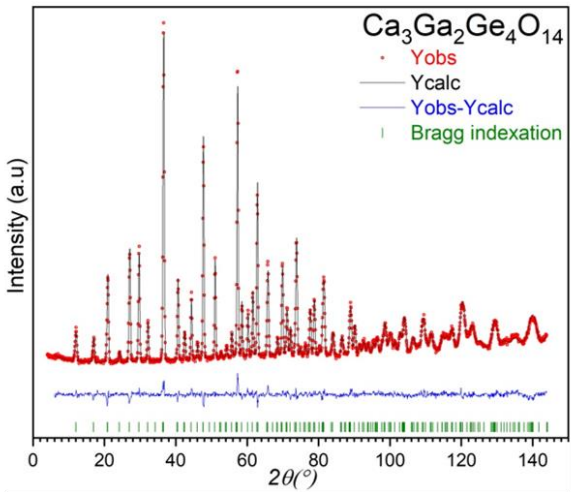

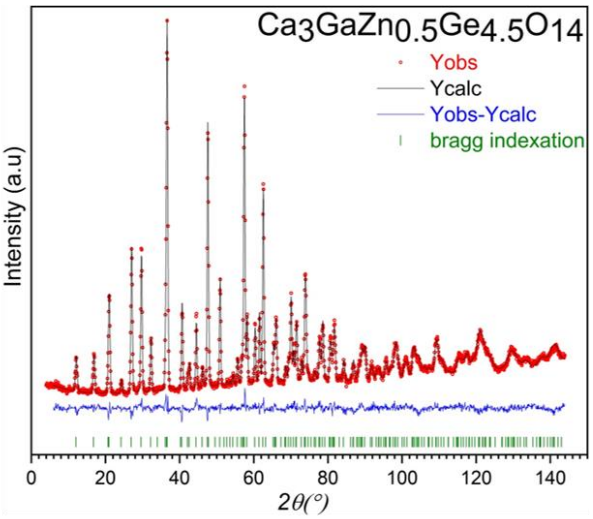

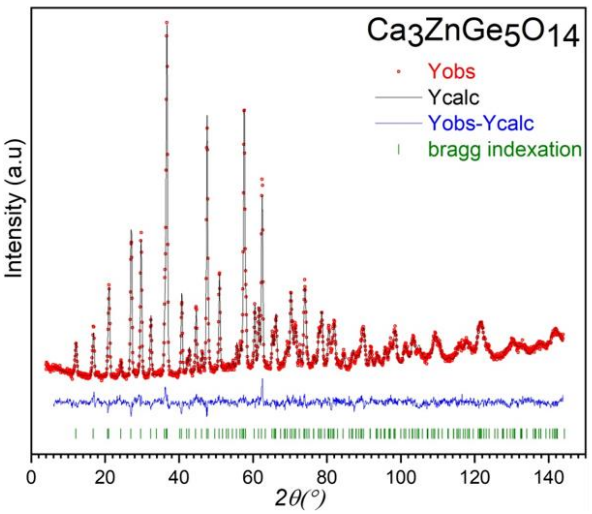

x=0 Sample			x=1 Sample		
Atom	Site	Occ	Atom	Site	Occ
Ga1	1a	0.507(81)	Zn1	1a	0.472(37)
Ge1	1a	0.493(81)	Ge1	1a	0.528(37)
Ge2	2d	1	Ge2	2d	1
Ga3	3f	0.498(27)	Zn3	3f	0.176(12)
Ge3	3f	0.502(27)	Ge3	3f	0.824(12)

Structure determination of Ca2ZnGe7O17

Neutron Physics Laboratory - Neutron diffraction

Mathieu ALLIX

Proposal ID

517

Report regarding proposal "Structure determination of $Ca_2ZnGe_7O_{17}$"

S. Chenu, E. Veron, C. Genevois, M. Pitcher, M. Allix, CNRS, CEMHTI UPR3079, Univ. Orléans, F-45071, Orléans, France
P. Beran, Nucl. Physics Inst., Rez, Czech Republic

Using glass crystallisation from a CaO-ZnO-GeO2 glass, we have synthesised a new material, namely $Ca_2ZnGe_7O_{17}$. Neutron powder diffraction data measurements were performed to complete a preliminary model based on laboratory X-ray diffraction and high resolution and HAADF-STEM imaging.

The extracted data is still under evaluation but preliminary results already led to a decent model which will be optimized further. See the fitted NPD data below:

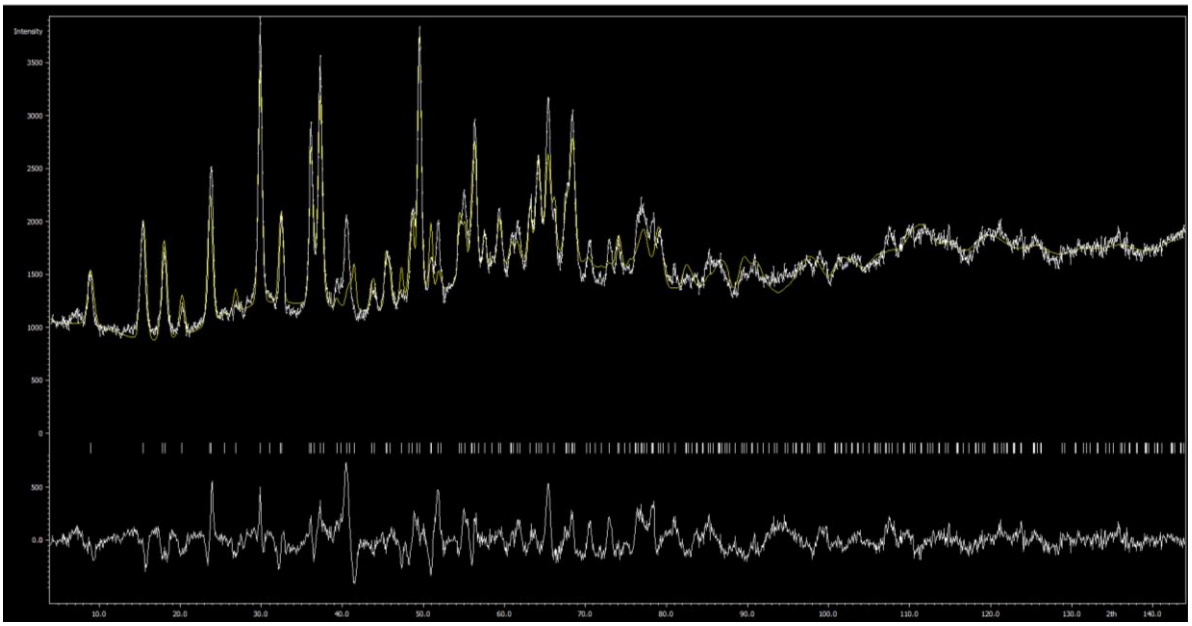

Preparation of the Ni binary layers suitable for the formation of graphene

Laboratory of Tandetron

Romana Mikšová

Proposal ID

519

Report regarding proposal "Preparation of the Ni binary layers suitable for the formation of graphene"

Romana Mikšová [a], Adéla Jagerová[a,b], David Poustka[c], Anna Macková[a,b]*

[a]Nuclear Physics Institute CAS, 250 68 Rez, Czech Republic; [b]Department of Physics, Faculty of Science, University of J. E. Purkyně, Pasterouva 3544/1, 400 96 Ústí nad Labem, Czech Republic; [c]Centre for Nanomaterials and Biotechnology, Faculty of Science, J. E. Purkyně University in Ústí nad Labem, Pasteurova 3544/1, 400 96 Ústí nad Labem, Czech Republic

Thin bimetallic Ni-Au layers (~100 nm) with three different Au content were prepared by direct current magnetron sputtering onto sapphire substrates. The elemental composition and the layer thickness of bimetallic layers were controlled during the sputtering process. The prepared Ni-Au layers were annealed at temperatures of 400°C and 900°C in the air to determine the behaviour of Au and Ni in the layers after heating. The elemental composition and depth profiling was provided by Rutherford backscattering spectrometry (RBS) (Figure a). The surface morphology was examined via Scanning electron microscopy (SEM).

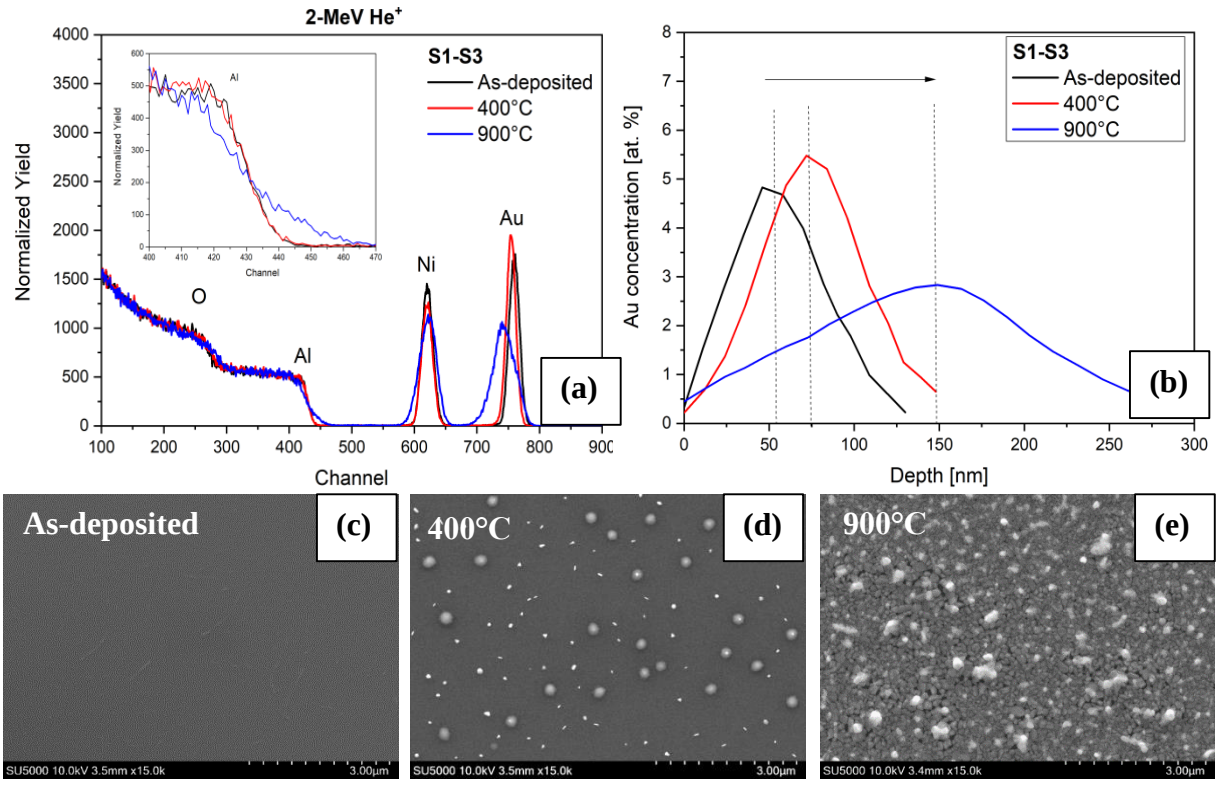

RBS measurements show Au and Al_2O_3 inter-diffusion, especially after annealing at 900°C (Figure b – blue line). Blister formation is shown in sputtered Ni-Au thin layer after annealing (Figures d and e) which is connected to the out-diffusion of the trapped sputtering gas after thermal annealing. It is shown that blister size is reduced by increasing the sputtering pressure. Changes in the surface morphology are connected to the formation of grain and voids, where increasing the Au content in the layers results in larger grain on the sample surface.

The part of the results was published published in Radiation Effects and Defects in Solids. The next manuscript will be published in Vacuum at the beginning of 2023.

Study of strain-induced martensitic transformation in Co-28Cr-6Mo alloy prepared by 3D printing

Neutron Physics Laboratory - Neutron diffraction

Michaela Roudnicka

Proposal ID

521

Report regarding proposal "Study of strain-induced martensitic transformation in Co-28Cr-6Mo alloy prepared by 3D printing"

M. Roudnicka, J. Drahokoupil, Institute of Physics of the CAS, Prague, Czech Republic
Ch. Hervoches, Nucl. Physics Inst., Rez, Czech Republic

Co-28Cr-6Mo alloy prepared by Selective Laser Melting (SLM), one of the 3D printing techniques, has proved to be very susceptible to strain-induced martensitic transformation (SIMT). Metallographic operations for sample preparation (cutting, grinding, polishing, etching) significantly affected the fraction of the martensitic hcp phase analyzed by XRD (see Table 1, as-built material). Strain imposed into the material during cutting and grinding induced an extensive SIMT. Further operations (polishing and (electro)chemical etching) managed to partially remove the affected surface layer. After heat treatment (HT), the susceptibility to SIMT changed. Conventional solution annealing at 1200 °C/2 h preserved the tendency to SIMT but weakened its extent. HT at 900 °C/5 h, applied to stabilize the hcp phase, prevented SIMT completely and samples showed a constant hcp fraction regardless the applied steps of metallographic preparation.

Tab. 1 Hcp phase fraction (vol%) in different preparation stages of Co-28Cr-6Mo alloy determined by XRD

Stage of metallographic preparation	As-built	HT 1200 °C/2 h	HT 900 °C/5 h
Ground	44	25	83
Polished	28	18	83
Chemically etched, 5 min	24	12	83
Chemically etched, 10 min	22	11	83
Electrochemically etched, 5 min	9	2	80
Electrochemically etched, 10 min	7	2	80

Neutron powder diffraction experiments were performed on original as-printed samples without further intervention using the MEREDIT instrument. Samples in the as-built state and two heat-treated states (1200 °C/2h, 900 °C/5 h) were measured. The motivation for the experiments was to investigate the accurate phase composition of the 3D-printed Co-28Cr-6Mo alloy unaffected by any mechanical straining.

Neutron diffraction (spectra presented in Fig. 1) confirmed that the real hcp contents in the tested samples correspond to those in the last step of metallographic preparation. As-built samples and solution annealed samples showed dominant fcc phase with very weak peaks of the hcp phase. An accurate quantitative evaluation of weak peaks could not be done due to a strong background but the hcp content in as-built samples can be determined as 5–10% and <5% for HT 1200 °C/2 h samples. After 900 °C/5 h HT, the hcp/(hcp+fcc) fraction was determined as 83%.

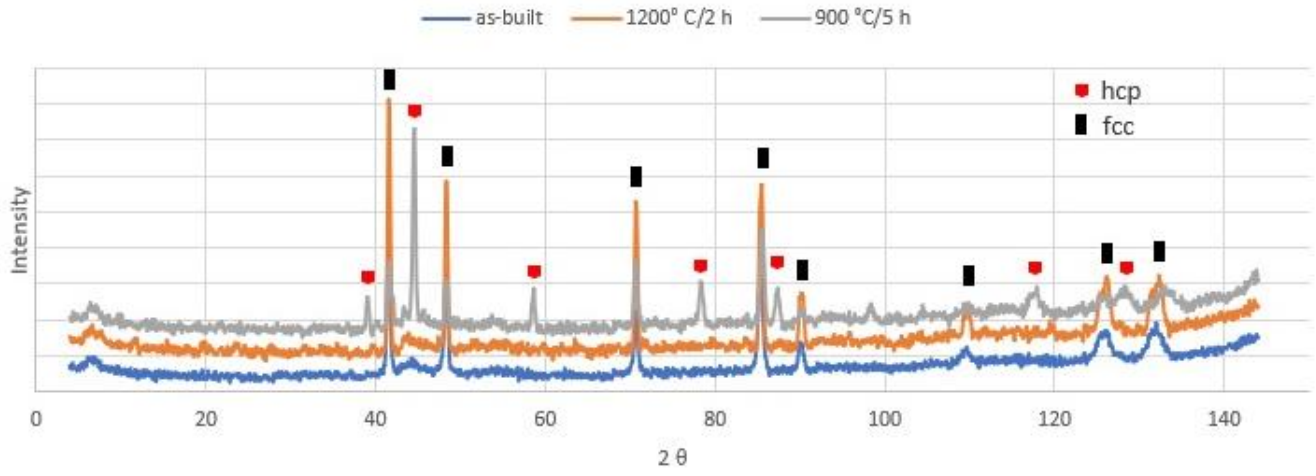

Fig. 1 Neutron diffraction spectra for as-built and heat-treated samples of Co-28Cr-6Mo alloy